STUDY OF OPTIMAL DEPOSITION CONDITIONS FOR AN ICP-CVD SYSTEM

MASTER OF ENGINEERING (2005) MCMASTER UNIVERSITY
(Department of Engineering Physics) Hamilton, Ontario

TITLE: Study of Optimal Deposition Conditions for an Inductively Coupled Plasma Chemical Vapour Deposition (ICP-CVD) System

AUTHOR: Haiqiang Zhang, B.Eng. (Tsinghua University)

SUPERVISOR: Professor P. Mascher

NUMBER OF PAGES: xii, 119

Acknowledgements

I would like to thank my supervisor, Dr. P. Mascher, for his support and encouragement during this thesis work. I want to thank him not only for the efforts invested in guiding and teaching me throughout the whole process of my master study, but also for his continued confidence in my ability and the research freedom he has allowed.

A special thanks goes to Dr. Jacek Wojcik, whose seasoned guidance, solid knowledge and rich experience in PECVD are of crucial importance in this project. Without his help, I would not be able to begin and make some progresses in this project. It was a great pleasure to work with him in the past two years.

In particular, I wish to thank Doris Stevanovic for her valued training and assistance when I used the clean room. In addition to giving me access to equipment for performing wafer cleaning, Doris also taught me a great deal regarding the safety and operation skills involved.

I would also like to thank Dr. Brad Robinson and Graham Pearson for their willingness to help whenever I needed it. Thanks are also due to Shawn Tan, Anna Villafranca for helping me use ellipsometers and other measuring equipment.

I must also thank my wife Julia. She has put as much work into this thesis as I have. She and my son Jerron have given me the inspiration and motivation to complete this thesis work.

Finally, I would like to thank the Canadian Institute for Photonics Innovations (CIPI), the Ontario Research and Development Challenge Fund (ORDCF) through the Ontario Photonics Consortium (OPC) and the Natural Sciences and Engineering Research Council (NSERC) for their financial support.

CONTENTS

List of Figures

List of Tables

Chapter 1

Introduction

The semiconductor industry follows a predictable trend – one where the transistor density doubles every generation, in about 3-year cycles. This has come to be known as Moore's Law [1]. Nowadays, in modern silicon integrated circuit (IC) technology, the dimension of the devices is aggressively scaled down for increasing packing density. Driven by the need of high-density, high-performance microelectronic products, thin film deposition technologies have been developed. Generally, thin film deposition processes play a critical role in the production of. Basically, thin film deposition technologies can be classified into four categories: (1) evaporative methods, (2) glow-discharge processes, (3) gas-phase chemical processes, (4) liquid-phase chemical techniques [1]. Among these technologies, plasma enhanced chemical vapour deposition (PECVD) is one of the most efficient technologies for the fabrication of semiconductor devices which are sensitive to high temperature.

Reducing the deposition temperature by the CVD process has been one of the intensive research objectives for several reasons [2,3]: (1) In modern IC industries, multi-metal-layers are often used in the fabrication of electronic devices. Dielectric films, such as silicon oxide or silicon nitride, which are needed for electrical isolation, have to be deposited at less than 400°C to prevent from affecting the underlying metal layer [4]. Traditionally these films used to be

deposited by low-pressure chemical vapour deposition (LPCVD) at temperatures above 700°C [4]. These relatively high temperatures are, however, not compatible with the thermal budgets in modern processes of large-scale integrated circuits. (2) In order to improve the functionality of devices, a wide range of materials are used as the substrate, such as plastics and polycarbonates [5]. These materials tend to melt at high temperature. (3) Deposition at low temperature can also reduce the stress evolution in the film caused by the different thermal expansion coefficients between the coated film and the substrate.

If, however, the CVD temperature is reduced to a certain value, say 400°C [4], the thermal energy is insufficient for the chemical reaction of concern. Then the energy difference has to be supplied from other energy sources, e.g. from an RF glow discharge in the reacting gas, to create a higher than equilibrium quantity of free radicals. In such a plasma-enhanced (PE) reaction, the flux of free radicals to the wafer surface at low temperature is thus sufficient to produce acceptable deposition rate.

The trend toward high-rate, single-wafer processing in integrated circuit (IC) fabrication has brought forward some new requirements including high densities of ions, electrons and radicals, excellent uniformity over diameters of at least 20cm, low and controllable ion energies and negligible contamination from reactor sputtering [6]. Fortunately, most of these requirements can be met by high-density plasma CVD (HDPCVD) using high-density plasma sources (such as electron cyclotron resonance (ECR), inductively coupled plasma (ICP)). The

high-density plasmas allow high process rates at low pressures and more effective dissociation of the precursors, thus lower the deposition temperature [7].

Among the high-density plasma sources, an inductively coupled plasma source (ICPS) has been developed as a new plasma excitation method since the early 1990s [8]. The ICPS is very attractive from the viewpoint of the plasma processing. It employs a coil configuration to couple the RF energy to a cylindrical cavity and is capable of producing high-density plasmas ($> 10^{11}$ - 10^{12} cm^{-3}) at low pressures (< 1 - 20 mTorr) [9]. Furthermore, the ICPS allows processing of large size wafers with high uniformity [10,11] without the need for external magnetic fields, such as electron cyclotron resonance (ECR) sources. These characteristics of the ICPS are favourable for chemical vapor deposition of various high-quality films such as silicon oxide, silicon nitride, silicon oxynitride and others.

At McMaster University, in addition to an existing ECR-CVD system, a new ICP-CVD system has recently been constructed and installed aiming at further study of silicon-based thin films.

Silicon oxides, silicon nitrides and silicon oxynitrides have been widely used in the microelectronics industry for many years. Due to their properties of high mechanical hardness, high electrical resistivity, low friction coefficient, and chemical inertness, they have found a wide range of applications, including as intermetallic insulation [12] and passivation [13], and masks for local oxidation and selective doping [14]. Other specific applications include the use of silicon

nitride as gate dielectric in thin film transistors (TFT) [15,16] and as optical material [17].

The electrical and optical characteristics of the SiO_2, SiN_x, SiN_xO_y thin films deposited by ECR-CVD have extensively been studied by many researchers, however, only few researchers reported studies on ICP-CVD deposited thin films, probably because ICP-CVD is a relatively new deposition tool. In recent years, nanocrystalline semiconductor materials are under intensive study due to their potential applications in novel optical and electro-optical devices [18,19]. A lot of techniques, such as sputtering, laser-chemical vapor deposition (L-CVD), ion implantation, and plasma enhanced CVD, have been used for the preparation of films consisting of nanocrystalline Si embedded in a matrix of silicon nitride or oxide. Though very few people tried to use this method to grow nanocrystal material, ICP-CVD is believed to be a suitable and efficient tool for investigations in this area.

Conceptually ICP-CVD is somewhat simpler and more automated than other high-density plasma CVD techniques, such as ECR-CVD, but it is still a rather complicated big system. In order to make the system work to its highest efficiency, a careful and sophisticated calibration should be carried out before it is ready for research purposes. During a deposition process, a variety of parameters, such as substrate temperature, gas composition, flow rates, chamber pressure, RF power density, could affect the characteristics and quality of the deposited film. The purpose of this project is concentrated on the setup and calibration of the

ICP-CVD system. In this thesis, a detailed introduction to the components of this system as well as their functions, basic physical principles and background behind the operation will be given and the calibration work on temperature, film uniformity and refractive index will be described.

A good understanding of the mechanism of ICP is a key issue to comprehend the working principle of the whole system. After a brief review of inductively coupled plasma technology, the theoretical model of ICP sources along with some related important physical conceptions are given in Chapter 2.

Chapter 3 focuses on the description of the main components of the ICP-CVD system, such as the ICP source, the vacuum system, the gas delivery system, and the temperature measurement and control system.

In Chapter 4 a brief review of the principles and theoretical background of ellipsometry and a short introduction on the ellipsometers used in this project are provided.

Chapter 5 presents some experimental details for the deposition of silicon oxide, silicon nitride and silicon oxynitride films by ICP-CVD, including sample preparation, deposition methods and process control. Furthermore, deposition chemistry and reaction mechanisms of the processes are also described in this section.

In Chapter 6, the calibration work on the system are analysed and discussed. Several important results with respect to the actual temperature of the substrate, deposition conditions for optimal uniformity, relationships between the

deposition rate and processing variables, and refractive indexes of thin films under different deposition conditions are presented and discussed.

Finally, the conclusions of this thesis are summarized in Chapter 7 and some recommendations are made for further research.

Chapter 2

Inductively Coupled Plasma Sources

2.1 Introduction

Although inductively coupled plasmas (ICPs) have been generated and studied for over 100 years, the application of ICPs has for a long time been confined to make plasma torches that can be used in conjunction with other analytical instruments, such as Atomic Emission Spectroscopy (AES) [20] and Mass Spectroscopy (MS) [21]. From the mid to late 1980s, inductive systems started to be used in plasma processing. The use of inductive plasmas may have been delayed by the fact that systems which look "inductive" actually run in a capacitively coupled mode thus do not exhibit the high efficiency and high plasma density capabilities at low pressure of present inductively coupled plasmas [22]. Nowadays, ICP sources have been able to produce high-density and large-diameter plasmas at low pressure. The main advantages of the ICP-CVD system over conventional PECVD systems are the high-density plasma, low deposition pressures and temperatures. These advantages will lead to minimize film contamination, promote film stoichiometry, reduce radiation damage caused by direct ion-surface interaction, and eliminate device degradation at high temperatures. The ICP-CVD also has other advantages, such as no magnetic field

on the wafer processing position, easy production of large-diameter uniform plasmas, a compact and simple source.

In this project, an ICP-CVD system has been set up at McMaster University. The core component is a RF 6.02 plasma source, which is capable of generating a 3 kW, 13.56MHz radio frequency signal, to produce an inductively coupled plasma with relatively high ionization efficiency. In this chapter, we start from some important conceptions of plasma physics, followed by a historical evolution of ICP technology and classification of most frequently used ICP sources. Finally a transformer model is described to illustrate the mechanism of the plasma generation.

2.2 Important Concepts

2.2.1 Plasmas

In addition to three states of matter such as solid, liquid and gas, plasma is often referred to as the fourth state of matter by most physicists, even though there still exist some arguments. The name of "plasma" comes from the Greek word "πλασμα", which means something molded or fabricated [23]. The Nobel prize-winner, American chemist Irving Langmuir, first used this term to describe an ionized gas in 1927. A useful definition is that a plasma is a partially ionized gas consisting of equal numbers of positive and negative charges, and a large number of un-ionized neutral molecules [24].

As we know, a solid substance generally passes through a liquid state into a gas state, and then decomposes to form a gas of atoms when it is heated to a

sufficient high temperature. If the temperature is further increased, atoms decompose into negatively charged electrons and positively charged ions, and the substance enters the plasma state. This plasma is referred to as hot plasma or fusion plasma, which is characterized by high ionization (almost fully ionized) and in thermal equilibrium. That is to say, the temperatures of all the species in the plasma are the same. In contrast to the hot plasma, a cold plasma can be created by using an exciting field to accelerate electrons, which then ionize the atoms. Shown in Figure 2.1 is a schematic of a simple ICP discharge.

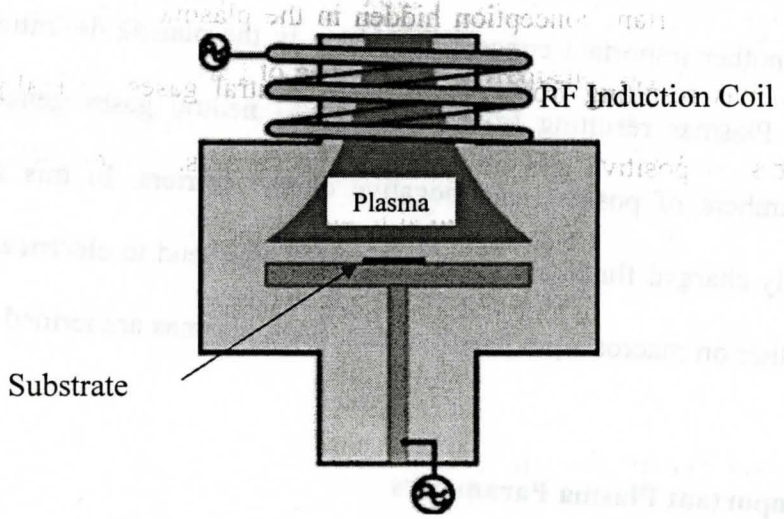

Fig. 2.1 Schematic of a simple ICP discharge

It consists of a dielectric chamber surrounded by a solenoidal coil. Simply speaking, the radio frequency (RF) currents in the coil (inductive element) generate an RF magnetic flux. The time-varying magnetic flux induces a solenoidal RF electric field, which accelerates the free electrons to break down gas atoms/molecules, resulting in formation of a "cold" plasma. Unlike a hot

plasma, which is nearly fully ionized, the cold plasma is usually weakly ionized, that is, in the plasma flux, only a small fraction is ions and electrons, most are neutral particles. Secondly, the temperatures of the different plasma species are not the same; more precisely, the electrons are characterized by much higher temperatures (on the order of 50,000K [25]) than the heavy particles (ions, atoms, molecules). This difference between electron and heavy-particle temperatures makes cold plasmas of great interest for planar processing, and in particular for plasma-enhanced chemical vapour deposition (PECVD).

Another important conception hidden in the plasma definition is "quasi-neutral". Plasmas resulting from ionization of neutral gases generally contain equal numbers of positive and negative charge carriers. In this situation, the oppositely charged fluids are strongly coupled, and tend to electrically neutralize one another on macroscopic length-scales. Such plasmas are termed quasi-neutral [26].

2.2.2 Important Plasma Parameters

The following section provides a description of the most important parameters that determine the characteristics of a plasma.

- **Plasma temperature**: As mentioned above, at high pressure, a hot plasma is in thermal equilibrium, so the ion temperature is the same as the electron temperature. But in a weakly ionized cold plasma, or in a hot plasma at low pressure, electrons and ions are never in thermal equilibrium. Because the mass of ions is many times bigger than that of electrons, light electrons move much faster

in plasma than heavy ions, the applied power to generate plasmas preferentially heats the mobile electrons, leading to a much higher electron temperature in contrast to a low ion temperature. Whether or not a plasma is in thermal equilibrium, the kinetic temperature of species in a plasma can be denoted as:

$$T_s = \frac{1}{3} m_s v^2 \qquad (2.1)$$

Here, v is a particle's speed. The kinetic temperature of species s is essentially the average kinetic energy of particles of this species.

- **Plasma frequency**: Every kind of plasma has a particular oscillation frequency, which is referred to as the plasma frequency ω_p. It is one of the most fundamental characteristics of plasmas. Although the electrons and ions in a plasma are in equilibrium as a whole, it is just the average result of many detailed interactions. At short time scales, the plasma is always perturbed from neutrality for certain reasons. Then, there will be large restoring forces striving to re-establish charge neutrality. These restoring forces are proportional to displacement, which is the condition for oscillations, consisting of electron oscillation and ion oscillation. The frequency of oscillations is the so-called plasma frequency ω_p.

A simple way to understand this conception is to consider a neutral plasma, consisting of a gas of positively charged ions and negatively charged electrons, which is given an initial perturbation by displacing all of the electrons from their quasi-neutral positions by a tiny amount with respect to the ions. We know that

ions and electrons are by no means free in a plasma, there exists a strong Coulomb force between the negative and positive collective assemblies. The Coulomb attraction will pull back those electrons to their original positions. But their inertia would carry them far away again from the balance positions, and then electrons being pulled back again by attraction. Thus the whole process repeats leading to an oscillation with an oscillation frequency.

Though both electrons and ions could oscillate in the plasma, the large mass difference between ions and electrons ensures that ion oscillations are so slow that thermal equilibrium is mainly maintained by electron oscillations. So we usually ignore the ion oscillations' contribution, and define the plasma frequency ω_p in terms of the electron plasma frequency:

$$\omega_p = \sqrt{\frac{ne^2}{\varepsilon_0 m}} \tag{2.2}$$

where n is the electron density, ε_0 is the permittivity of free space, m is the mass of an electron and e is the charge of the electron. Note that the relation (2.2) is given under the assumption of infinite ion mass, which is reasonable in a cold plasma. As for a hot plasma, the expression of (2.2) should be modified, but this is beyond our concern in this thesis.

- **Plasma Sheaths**: Once a plasma is generated in a chamber, people usually observe a dark space between the bright bulk plasma and the chamber wall. Goeckner [27] found that in this dark space not only electron density is extremely low, there also exists an electric field pointing from the plasma towards the wall.

Actually this phenomenon can be observed adjacent to all surfaces in contact with the plasma. The dark space is referred to as plasma sheath. To know why, let's suppose initially that in the space adjacent to the chamber wall, the electron density is equal to the ion density due to quasi-neutrality. Ions and electrons will fly out of the plasma, hit the wall, recombine there and then get lost. The electron thermal velocity $V_e = \left(\frac{3T_e}{m}\right)^{1/2}$ is at least 100 times the ion thermal velocity $V_i = \left(\frac{3T_i}{M}\right)^{1/2}$ because M/m >> 1, $T_i << T_e$. (Here, T_e and T_i are the temperatures of the electrons and ions respectively, m and M are the masses of the electrons and ions respectively.) [25]. Since electrons have much higher thermal velocities than ions, on a very short timescale, electrons near the wall are lost faster, leading to the formation of a sheath between the plasma and the wall, in which $n_i >> n_e$. The net positive charges within the sheath generate an electric field (or a confining potential), which on the one hand confines electrons to fly to the wall, on the other hand accelerates ions towards the wall until a charge balance is obtained. The potential across the sheath in an ICP is typically of 10-25 volts. The sheath potential in a capacitive plasma is much larger: it varies during the RF cycle, with peak values of several hundred volts often present [28]. Fig. 2.2 shows the formation of plasma sheaths in a plasma chamber.

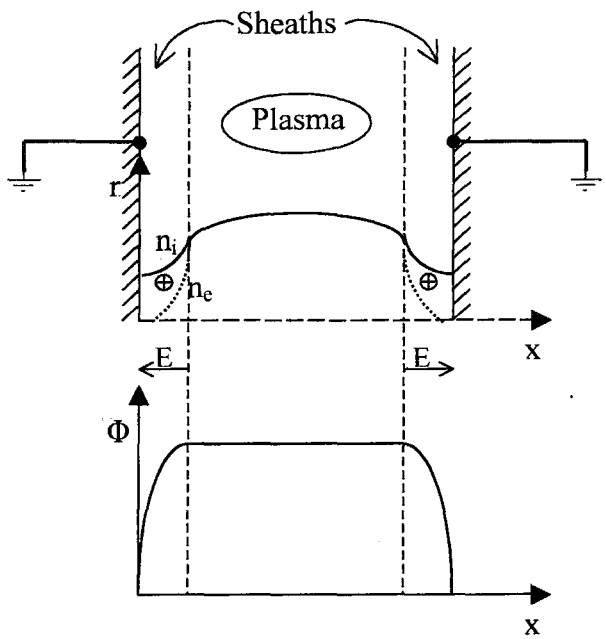

Fig. 2.2 The formation of plasma sheaths. [25]

Since electrons in the plasma cannot enter into the sheath region due to the potential barrier, though occasionally an ion striking the wall surface might knock off an electron -- a secondary -- which then is accelerated into the plasma by the sheath electric field, there are actually very few electrons within the sheath. This lack of electrons results in low levels of excitation of the gas species in the region and, hence, as noted above, the area appears dark.

- **Skin Depth:** High frequency signals, such as electric field, magnetic field or both, cannot penetrate far into a good conductor like metals, because the resistance associated with a conductor at these high frequencies will be higher than the dc resistance. This effect is known as the skin effect since the high frequency current flows in a thin layer near the surface of the conductor. The depth to which the electromagnetic wave penetrating into a conducting surface

has fallen to e^{-1}, about 0.37, of its original level, is conventionally defined as the skin depth. The well-known equation for the skin depth is given below:

$$\delta = \sqrt{\frac{2}{\mu_0 \omega \sigma}} \tag{2.3}$$

where δ is the skin depth. It is a function of three variables: the permeability μ_0, the angular frequency ω and the electrical conductivity σ.

Equation (2.3) presents clearly that the skin depth is inversely proportional to the square root of the frequency; that is to say, the skin depth shrinks with increasing frequency. Also one can find that the skin depth decreases when the conductivity increases. It will approach 0 as $\sigma \to \infty$, since in that case the charges are infinitely mobile and hence free to move around and reorient themselves so as to completely exclude the electric field. For finite conductivity the skin depth is finite and depends on frequency as $1/\sqrt{\omega}$. This implies that high frequency waves stay on the surface of a conductor.

A plasma has a high conductivity because it contains inside a large number of freely travelling electrons. Actually a plasma can in a certain sense be considered as a conductor. So one will expect an electromagnetic field to behave similarly in a plasma as it propagates in a metal conductor. Just as in a metal, electromagnetic fields at low frequencies cannot propagate in a plasma, but are reflected; at too high frequencies the plasma electrons cannot respond and fields travel freely. The boundary between these regimes is the plasma frequency ω_p, which was discussed earlier. Waves with frequency near the plasma frequency

decay over a skin depth into the plasma. The skin depth for electromagnetic fields penetrating into a plasma has the same form as (2.3), which is $\delta_{plasma} = \sqrt{\frac{2}{\mu_0 \omega \sigma}}$, just that in the expression, σ is the plasma conductivity.

2.3 Principles of ICP Source Operation

2.3.1 Typical High Density Plasma Sources

It has been known for over a century that a gas discharge containing charged (ion) and neutral (radical) species can be used to initiate chemical processes. In 1962, Anderson [29] first found in his experiment that a radio frequency (RF) could be applied inside a glass tube to generate active species for thin-film deposition. Since then a large variety of plasma sources has been developed to create gas discharge plasmas, employed in plasma-enhanced CVD (PECVD). In recent years, new materials requirements and lower-processing-temperature requirements in modern microelectronic industries have stimulated the need for high-density plasma sources (HDPS). The new generation of HDPS is characterized by low pressure (typically 1~75 mTorr), by higher plasma densities (typically 10^{11}~10^{13} cm^{-3}) and good uniformity over large surfaces (e.g. 20~30cm diameter) at these low-pressure conditions [30]. Generally speaking, these high-density plasma sources can be classified into five categories [31]:

1. Capacitively coupled plasma sources
2. Inductively coupled plasma sources
3. Helicon plasma sources

4. Surface wave plasma sources
5. Microwave plasma sources

Compared with other high-density plasma sources, the RF driven, inductively coupled plasma is one of the oldest plasma generating methods which is well known for its simplicity and high efficiency, and has a wide range of industrial uses. As we know, due to technical limitations and discharge mechanisms which are not well known, the most common application for ICPS has for a long time been restricted to make plasma torches for spectral analysis [31]. In PECVD one has traditionally used capacitively coupled plasmas for deposition and etching applications. With the development of plasma physics, and the need for large-area, high-density plasma sources for plasma-aided manufacturing of integrated circuits, inductively coupled plasma sources (ICPS) have recently re-attracted more attention and become one of the promising candidates for meeting the future needs of IC. A brief review of inductively coupled plasmas is indispensable for better understanding of this "old but new" chemical vapour deposition tool.

2.3.2 Historical Review of ICP Sources

Inductively coupled discharges are nearly as old as the invention of electric power. The first experimental research in electrodeless gas discharges was reported by Hittorf in 1884 [32]. He wrapped a coil around an evacuated tube and then observed that residual gas in the tube begins to glow as soon as a high frequency current is passed through the inductor. In the beginning, these

discharges were explained by the action of the electrical field between the turns of the inductor Some others like J.J Thomson, argued that this form of discharge was not caused by the electric, but by the magnetic field of the inductor, and had the nature of an induction current in the gas. In the 1920's, J.S. Townsend and R. H. Donaldson [33] pointed out that the electric field strength between two ends of the solenoid is 30 to 40 times higher than the electrical field strength induced by the alternating magnetic field, and the geometry of this field can produce a discharge in circular form. Later experiments showed that two types of discharges caused by the electric and magnetic fields can exist in a vacuum cylinder placed into a high frequency inductor Later, G I. Gabat [34] called them the H-discharge and the E-discharge.

A subsequent 50-year controversy developed as to whether these discharges were capacitively driven by plasma coupling to the low- and high-voltage ends of the cylindrical coil, as in a capacitive discharge, or were driven by the induced electric field inside the coil. Present understanding of the nature of high frequency electrodeless discharge consists of the following [31]

The electric field between the extreme turns of the solenoid coil creates the initial ionization of the gas, and leads to a weak discharge. The ionization increases with an increase in the amplitude of the high frequency oscillations, thereby increasing the conductivity of the discharge. Initially the discharge conductivity is low, which makes it transparent for the H-field. So the alternating magnetic field of the inductor cannot transfer its energy to the discharge. The

source operates in the capacitive regime, which is often referred as the E-mode. However, when the conductivity under the effect of an increase in the E-field reaches a certain threshold, the magnetic energy of the inductor starts to be transferred, beginning the H-form of the discharge. In conclusion, the discharge is capacitively driven at low plasma densities, with a transition to an inductive mode of operation at high densities. More details will be discussed in Section 2.3.4.

2.3.3 Classification of ICP Sources

Typical ICP sources can be classified into five types according to their geometrical features, which include [6]:

(a) helical inductive couplers-cylindrical plasmas: An induction coil is wrapped helically around a dielectric chamber. The induced electrical field within the plasma is azimuthal, and the RF magnetic field is directed along the central axis.

(b) helical resonators-cylindrical plasmas: This type actually belongs to the helical class. The only difference between this type and type (a) is that the length of the coil is designed to be ($\lambda/4 + n\,\lambda/2$) or ($\lambda/2 + n\,\lambda/2$), where n = 0, 1, 2, ..., λ is the wavelength of the excitation frequency. The former equation is for a quarter-wave resonator and the latter is for a half-wave resonator. A trimming capacitor is usually connected between the coil and ground to adjust the capacitance to ground such that the structure resonates.

(c) spiral inductive couplers-planar plasmas: A spiral-like coil is separated from the low pressure discharge chamber by a dielectric vacuum window. A capacitance in series with the spiral inductor is tuned to make the circuit resonate at the RF frequency. This source is characterized by generating a uniform plasma in a large planar area.

(d) immersed inductive couplers: Different from the above three types, the inductor is placed inside of the plasma vessel. This source is more suitable for the application of metal sputtering.

(e) transformer-coupled plasmas: A ring-shaped vacuum tube is placed in a ferrite core transformer which can couple low- or high- frequency energy into the tube chamber. This narrow cylindrical geometry is just suitable for laser design while not appropriate in semiconductor fabrication.

The ICP source used in our system belongs to the first type, and will be introduced in the next chapter.

2.3.4 Modeling of an ICP Source

The simplest and most efficient model of the ICP is known as the transformer model [35 - 37], shown in Fig. 2.3. In this model, the N-turn induction coil is considered the primary of the transformer while the high-density discharge or plasma is modeled as a single-turn secondary winding with a series-connected plasma impedance Z_{plasma}.

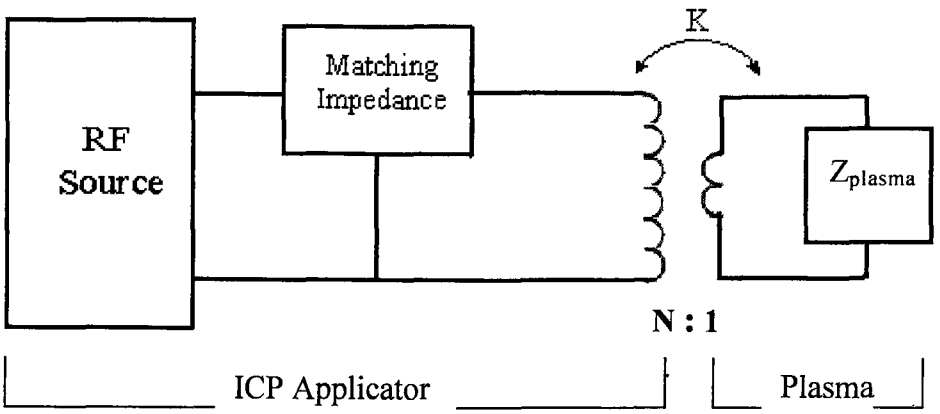

Fig. 2.3 Schematic of a classical transformer model

The equivalent circuit of this model is shown in Fig. 2.4. The primary coil impedance Z_c is composed of inductance L_0 and resistance R_0. The plasma impedance Z_{plasma} consists of two components, the inductance L_{pl} and a plasma resistance R_2, as seen in Fig. 2.4 (a).

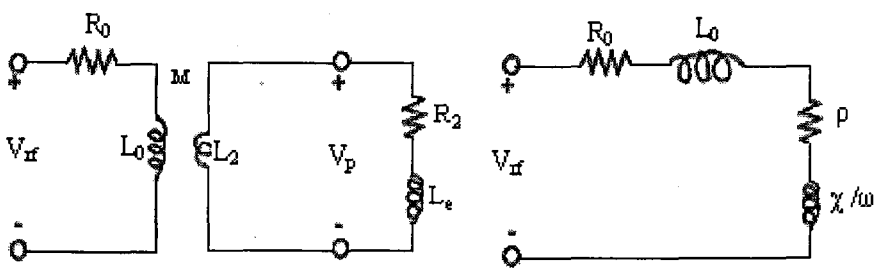

Figure 2.4 Equivalent circuit of the transformer model. (a) The primary circuit and the secondary circuit (b) The secondary circuit transformed into the primary circuit. [38]

In order to get a more precise agreement with experiments, the electron inertia term of plasma inductance should be taken into account, as was pointed out

by J.T. Gudmundsson [38]. So $L_{pl} = L_2 + L_e$, where L_2 is called geometrical inductance which is due to the plasma current path. L_e is the electron inertia inductance.

If we look from the side of the primary circuit, as shown in Fig. 2.4(b), the equivalent circuit impedance due to plasma loading is $\rho + j\chi$, in which ρ is the change of plasma resistance,

$$\rho = \frac{\omega^2 M^2 R_2}{R_2^2 + (\omega L_e + \omega L_2)^2} \tag{2.4}$$

where M is the mutual inductance between the primary and secondary circuit, and ω is the driving frequency.

The change of plasma reactance χ is given by :

$$\chi = -\frac{\omega^2 M^2 (\omega L_2 + \omega L_e)}{R_2^2 + (\omega L_e + \omega L_2)^2} \tag{2.5}$$

Combining (2.4) and (2.5), we obtain the primary coil impedance Z_c:

$$Z_c = R_0 + \rho + j\omega(L_0 + \chi) = [R_0 + \frac{\omega^2 M^2 R_2}{R_2^2 + (\omega L_e + \omega L_2)^2}] + j[\omega L_0 - \frac{\omega^3 M^2 (L_2 + L_e)}{R_2^2 + (\omega L_e + \omega L_2)^2}] = R_s + j\omega L_s \tag{2.6}$$

The absorbed power within the plasma is :

$$P_{abs} = \rho I_{rf}^2 \tag{2.7}$$

where I_{rf} is the rms current flowing in the induction coil.

The voltage drop between the two ends of the primary induction coil is given by:

$$V_{rf} = I_{rf} Z_c. \tag{2.8}$$

So far, a transformer model for an inductively coupled plasma has basically been set up. Based on this model, interesting plasma characteristics, such as plasma resistance, inductance, and plasma conductivity, can be obtained by measuring the electrical parameters, e.g. I_{rf} and V_{rf} [39]. A more precise analysis should take into account the parasitic capacitances between the coil and the plasma and between each turn of the coil, as proposed by Pascal Colpo [40]. However, the transformer model is sufficient to relate external circuit parameters to the plasma impedance, but not to describe the fields within the plasma. More sophisticated electromagnetic models [37,38,41] have been developed to describe the induction fields within the discharge, but will not be further discussed here.

2.3.5 Electrostatic to Electromagnetic Mode Transition

Initially, as the excitation RF power is increased from zero to a low value (usually less than 100W), the gas first breaks down into a capacitively coupled plasma or E-mode. This is characterized by a low electron density ($10^8 - 10^{10}$ cm^{-3}) and a faint glow localized near the coil [42]. Although the RF current flowing in the induction coil can generate RF magnetic flux, and the time-varying magnetic flux then induces an azimuthal electric field E_θ, this field is so weak that it cannot produce ionization. The E-discharge is attributed to the longitudinal electric field strength caused by the voltage drop across the induction coil. In practice, a matching network is used to tune the inductor so that an electrical resonance at the RF driving frequency can be obtained. Under this resonant condition, the coil voltage is extremely high, thus the field between the inductor

and the gas is strong enough to create the initial ionization of the gas. Since the conductivity of the gas is small, the discharge is transparent for the electromagnetic field, and the alternating magnetic field of the inductor cannot transfer its energy to the discharge. In this case, the capacitively induced plasma is just maintained by the electric field. That is why we call it E-mode.

As the power continues to increase, the RF current in the induction coil as well as the azimuthal electric field E_θ increase, thus result in an increase of ionization of the gas and the conductivity of the plasma. Above a certain threshold current, an abrupt transition to the electromagnetic mode (H-mode) occurs. This transition appears as a sharp increase in the luminosity and the electron density ($10^{10} - 10^{12}$ cm^{-3}) in the discharge [42]. From this point on, the plasma is mainly sustained by the induced azimuthal electric field E_θ. This operation mode is called electromagnetic mode or H-mode.

The dynamics of the E to H transition was described qualitatively by Kortshagen *et al* [43] as follows: starting with an E-mode plasma and increasing the RF current in the induction coil, a value is reached where the induced electric field can produce ionization. At this point the ionization rate suddenly becomes higher than the loss rate, power balance no longer holds and n_0 (electron density) starts to increase. Since the effectiveness of the inductive power deposition increases linearly with n_0 (at low n_0), a higher amount of power is absorbed with increasing n_0, and the electron density will continue to rise. At a high enough n_0, the skin effect becomes significant. The inductively absorbed power grows more

slowly than n_0 and a new steady-state H-mode discharge, satisfying the power balance, is finally reached. Thus a stable H-mode discharge forms when the skin depth becomes smaller than the typical dimension of the vacuum chamber.

Amorim [44] reported an observation of abrupt increase in the plasma density when the rf power was increased from 50W to 400W (see Fig. 2.5).

The plasma density versus power in Fig. 2.6 shows discontinuous transition from a low-density mode where $n_0 < 10^{11}$ cm^{-3} to a high-density mode where $n_0 > 10^{12}$ cm^{-3}. The authors attributed this phenomenon to a transition from a low density E-discharge to a high-density ICP (H-discharge).

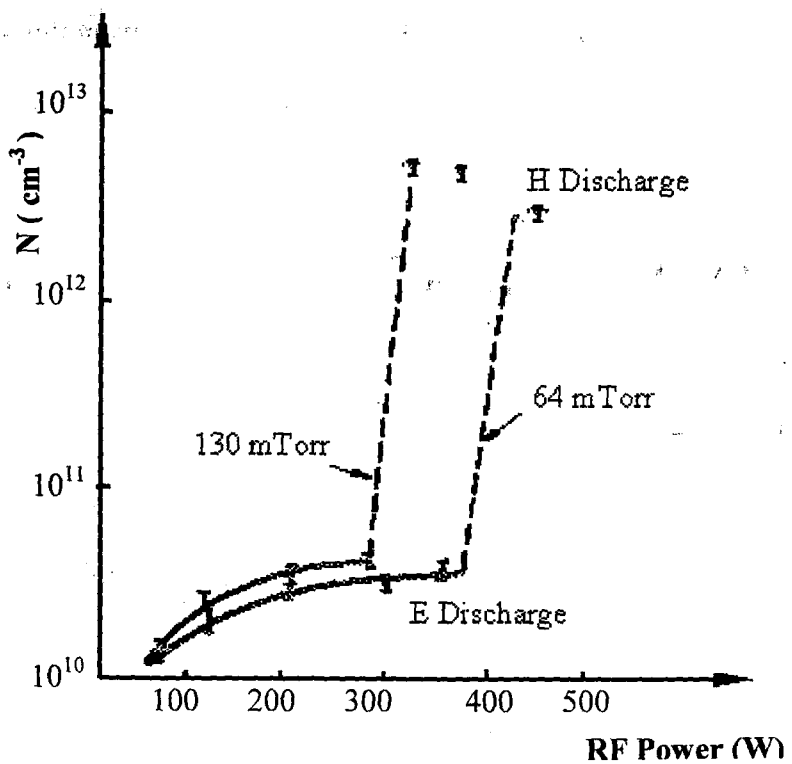

Fig. 2.5 Variation of the plasma density with RF power and the transition from the E- to the H- mode of the discharge. Data and graph taken from [44].

Chapter 3

The ICP-CVD System

3.1 Introduction

Inductively coupled plasma chemical vapour deposition (ICP-CVD) technology is a relatively new deposition tool, which can be used to deposit various kinds of materials on micro-sized regions of a wide variety of substrates. In this chapter, I will introduce a new ICP-CVD system at McMaster University. Functions and operational principles of some main components in this system will be presented.

3.2 The ICP-CVD system

The McMaster ICP-CVD system, as shown in Fig. 3.1, was built by Johnsen-Ultravac of Burlington, Ontario. The schematic diagram of this system is presented in Fig. 3.2.

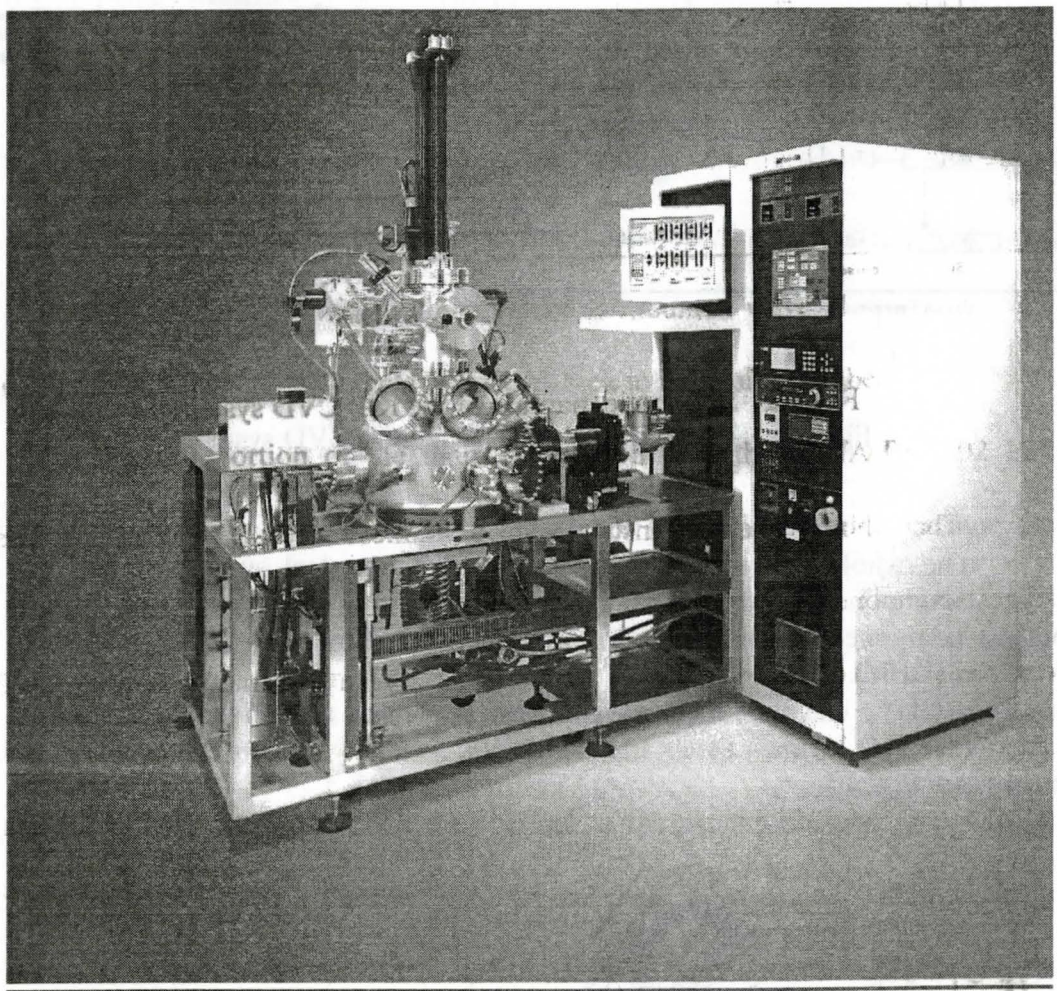

Fig. 3 1 The ICP-CVD system at McMaster University

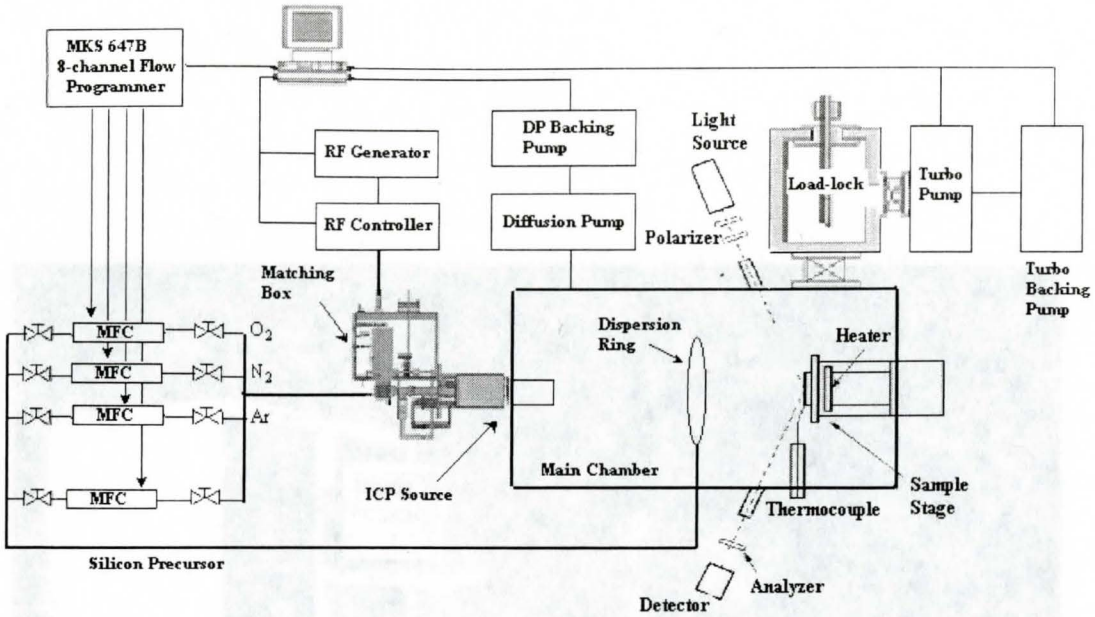

Fig. 3.2 Schematic diagram of the ICP-CVD system

The whole system is installed on a stainless steel support frame. The biggest component of the ICP-CVD system is an elliptically-shaped ultra high vacuum (UHV) chamber made of stainless steel with a diameter of around 22 inches (see Fig. 3.3).

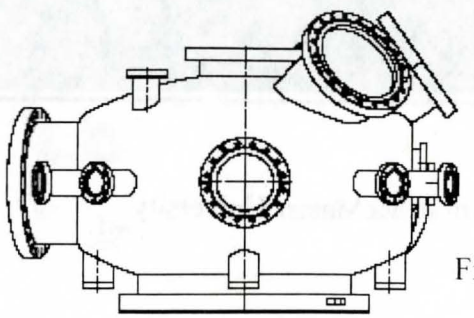

Fig. 3.3 Front view of the main chamber in the ICP-CVD system

It has a variety of ports for vacuum pumping, sample manipulation, gauging, gas introduction, view, ion gauges, crystal monitor, and ellipsometry.

Evacuating the main chamber is carried out by a diffusion pump, which is backed by a roots pump and a mechanical backing pump.

Atop the main chamber is a load-lock, which is used for loading/unloading samples so that the sample transfer time can be greatly shortened and the chamber contamination can be reduced during the sample transfer. The load-lock is pumped with a turbo pump backed by a turbo backing pump. A DC-motor-driven single-axis manipulator with 20-inch stroke is mounted vertically on top of the load-lock to transport the sample from load-lock to the main chamber.

The left portion of the main chamber houses the SVTA-RF-6.02 ICP source. A matching box is mounted outside of the main chamber to tune the reflected power to a minimum either manually or automatically. The centre part of the ICP source is a pyrolytic boron nitride (PBN) cylinder (plasma chamber) that is connected to a gas channel. All the plasma gases, namely O_2, N_2, Ar, are introduced horizontally through the channel to the plasma chamber and will be excited there to form a plasma. The plasma chamber is sealed with a ceramic cover, on which a lot of small apertures of different sizes are arranged in conformity with certain regularity (sometimes referred to as Aperture Pattern). The plasma generated in the plasma chamber diffuses through these apertures into the main chamber.

Inserted from the right side into the main chamber is a sample manipulator with ± 13mm travel and maximum 40mm Z motion. At the top section of the manipulator is a heating stage, on top of which the sample holder is clasped. The stage is heated by a planar-coil resistive heater and can be precisely maintained at temperatures up to 800℃. Because the heating stage is mounted on a rotary drive, the sample holder can be driven to rotate clockwise at a constant speed of 21 rpm during deposition, which is very important for the formation of a uniform film. A retractable thermocouple is installed on the side of the heating stage, which can be put forth to contact the sample holder so as to measure the substrate temperature.

In the middle of the main chamber, a circular dispersion ring is placed between the ICP source and the sample manipulator, through which silane (SiH_4) is introduced. The distance between the plasma source and the dispersion ring is 89mm. The closest distance from the dispersion ring to the sample is 44mm. This arrangement ensures that the reactions of chemical vapor deposition happen far from the plasma region so as to achieve a "clean" deposition with minimized plasma damage on the surface of the substrate. A rotatable shutter is used to shield the substrate surface from coating while one adjusts gas flow rates and ICP reflected power prior to the actual deposition.

The vacuum conditions are monitored by a Granville-Phillips Cluster Gauge System [45], which consists of two 316 vacuum gauge controllers to control four Convectron gauge modules (pressure range 1×10^{-4} to 999 Torr) - one for measuring the main chamber pressure, one for the load-lock, the other two for

monitoring the pressure inside the diffusion backing pump and turbo backing pump, respectively, and one 360 Stabil-Ion® Vacuum Gauge Controller, controlling two Stabil-Ion gauges (pressure range 1×10^{-4} to 2×10^{-10} Torr), providing real time pressure indication of UHV in main chamber and load-lock.

The gas flow package consists of eight separate channels with eight MKS 2179A mass flow controllers to accurately measure and control the mass flow rate in each channel. Currently, six gas channels are used in our system, while two channels are reserved for future use (For details see section 3.2.3).

Mounted on either side of the main chamber are the detector/analyzer and polarizer assembly of a J.A. Woollam M-44® in-situ spectroscopic ellipsometer, providing real-time measurements of thickness and refractive index of the deposited thin film during the process.

The ICP-CVD system mainly consists of five parts:

a) ICP source, including RF generator, plasma controller and matching system;
b) Vacuum system;
c) Gas delivery system;
d) Reaction chamber and sample load/unload chamber;
e) Process monitoring and controlling system.

Some details of these five parts are as follows:

3.2.1 The ICP Source and The Matching System

The ICP plasma generating system consists of:

- AE RFXII 3000 Power Supply which can generate a 13.56 MHz radio frequency with power range of 0~3000W. The value of 13.56MHz is a frequency approved by international communications authorities at which one can radiate a certain amount of energy without interfering with communications.
- A ROBO-RF plasma controller;
- A RF 6.02 plasma source;
- A RF matching box;
- A plasma monitor;
- PC and some periphery parts / cables.

Fig. 3.4 (a) shows the inductively coupled plasma source used in the McMaster ICP-CVD system. A schematic of this ICP source is presented in Fig. 3.4 (b).

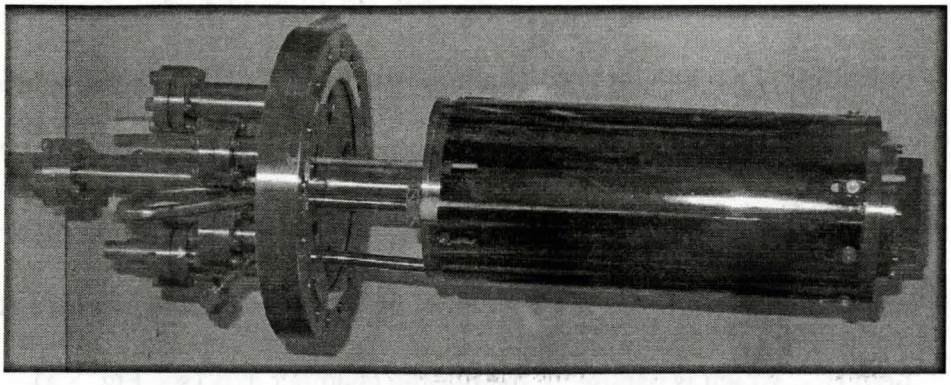

(a)

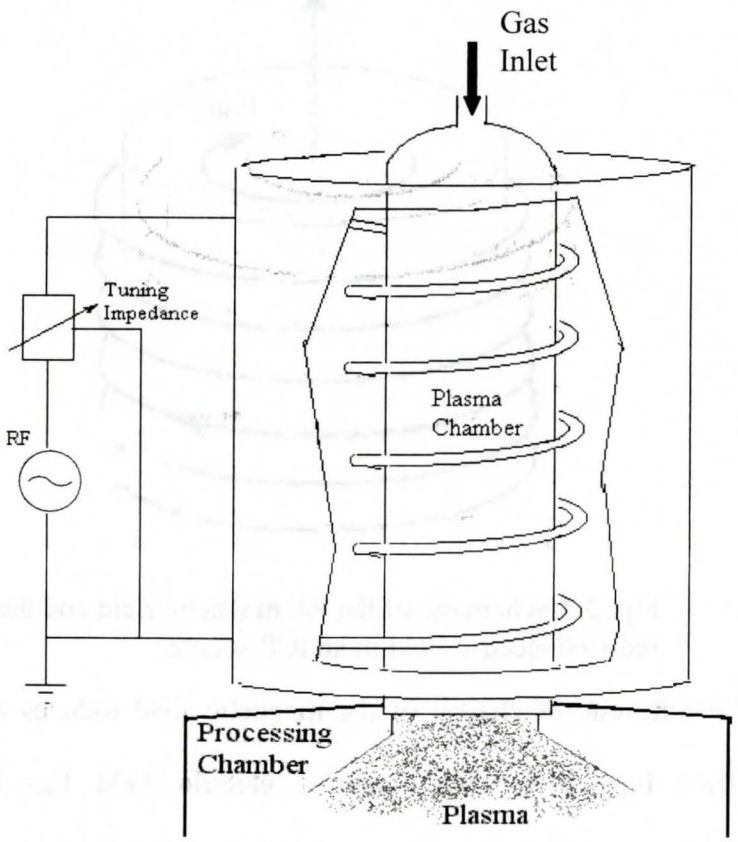

(b)

Fig. 3.4 The ICP source used in the ICPCVD system. (a) The ICP source (b) Schematic diagram of the ICP source

The outermost part is the RF shield, which functions to protect the surrounding equipment from the high RF field existing inside the source. Inside the shield is a spiral RF coil, which is wrapped around a PBN tube. This tube is the so-called plasma chamber, inside which a plasma is created. It is well known that large RF driven currents I_{RF} flowing in the coil can generate a RF magnetic field B_{RF}, which is parallel to the plasma chamber axis (see Fig. 3.5).

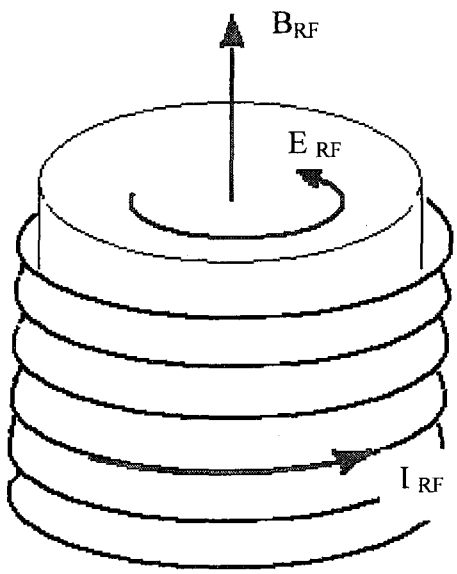

Fig. 3.5 Schematic of the RF magnetic field and the induced electric field in an ICP source

The time rate of change of the magnetic field induces a solenoidal RF electric field E_{RF}. It is this inductive electric field E_{RF} that induces a circumferential current in the plasma. The electrons thereby accelerated gain energy, creating enough hot electrons to sustain the plasma through ionization.

Once the plasma forms, there is a dark region – a sheath between the bright plasma region and the chamber wall. As described in Section 2.2.2, the

sheath region has much lower plasma density and cannot support much circumferential plasma current. So a visible plasma ring can be observed inside the sheath region. This visible ring is the region in which the plasma current flows.

The driven plasma ring extends into the central region of the chamber by a distance that can be characterized by the skin depth, as introduced in Section 2.2.2. Inside the current ring is the diffusion region. In the ICP sources, this region in the center of the chamber is field-free, not only E field-free, but also H field-free. We know that the plasma current can also generate a RF magnetic field, which is opposite to that generated by the coil. The cancellation of the two magnetic fields results in a damping magnetic field towards the central region. At the distance of skin depth inside the chamber wall, the magnitude of the magnetic field is reduced to 1/e of its original level.

Fig.3.6 (a) [46] & (b) show the structure and the equivalent circuit of the RF matching network used in the ICP-CVD system. From the above discussion, we know that the RF current could be very large. In order to avoid the possible damage that might be caused by too large RF current flowing round the circuit, the RF generator is designed to have a resistive output of 50 Ohms. RF discharge usually has a numerically larger and partly capacitive impedance, which cannot be adjusted without compromising the discharge process. Therefore, a matching network (with an adjustable capacitance) is used to combine the discharge load with the adjustable network load and tune the combined load to be equal to the generator output impedance during depositions so that a circuit resonance can be

achieved, and the power losses due to the large RF currents flowing between these two components can be avoided.

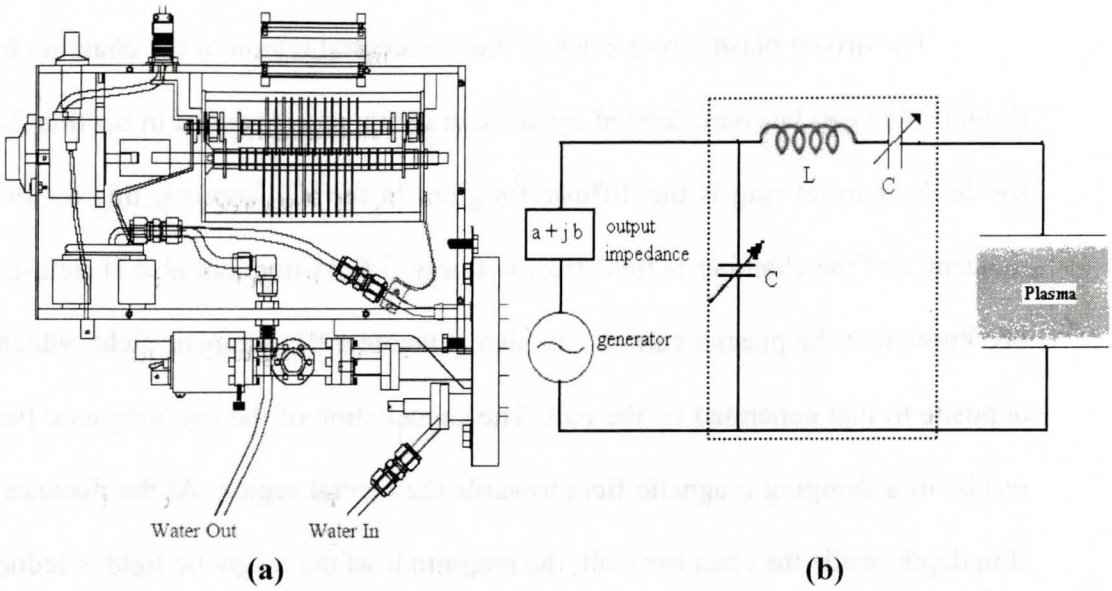

Fig. 3.6 The RF matching network. (a) RF matching box assembled in the ICPCVD system. [46] (b) Equivalent circuit of the RF matching network

3.2.2 Vacuum System

3.2.2.1 Introduction

Before deposition, the main chamber must be evacuated to a high vacuum due to the following reasons:

• On their way to the substrate, the reactant particles always collide with each other and then go in any and all directions. At low pressure, the electrons will not undergo many collisions with the gas atoms, and they will, therefore, be characterized by rather high energy, whereas the gas temperature remains low But if the pressure is high, e.g. at atmospheric pressure, on the other hand, the

electrons undergo so many collisions with the gas atoms that they tend to have only moderate energy (typical electron temperature 8000~10,000K), whereas the gas temperature is almost as high (typically 4500~8000K) [47]. Moreover, after losing too much energy by multiple collisions, many of the reactive species tend to react and condense to other solid particles before reaching the surface of the substrate.

- All the reaction by-products must be removed out of the reaction zone at a high rate during the deposition process. Otherwise they will increase the deposition system pressure and reduce the deposition rate significantly.

- At relatively high pressures, the collisions and reactions are so fast and dense that the deposition rate and quality are difficult to control.

An important question, however, is how good a vacuum is required.

The concept of mean free path (MFP) can be used to evaluate the proper vacuum pressure. Two equations were recommended by Ronald R. Willey [48] to calculate the MFP at room temperature:

$$MFP = \frac{5.0 \times 10^{-3}}{P(Torr)} cm \tag{3.1}$$

$$\frac{N}{N_0} = \exp\left(-\frac{x}{MFP}\right) \tag{3.2}$$

where P is the total chamber pressure in units of Torr. N_0 is the starting number of molecules. N is the number of molecules that have not collided after a distance x.

In our case, silane molecules introduced to the main chamber from the dispersion ring have to go over a distance of 4.5cm to reach the substrate. If the chamber pressure is maintained below 2 mTorr, the MFP is 2.5cm. Silane molecules will have a probability of about 83% to collide with other species in the plasma before they arrive at the substrate surface.

In order to achieve a reasonably high deposition rate, a significant amount of precursor species must flow through the reactor, but the system must be kept at low pressure constantly during the deposition. As a result, the required vacuum system must have a high pumping capacity and throughput. The vacuum system in our ICP-CVD system is composed of five vacuum pumps, as shown in Fig. 3.7.

The main component is a water-cooled Edwards EO9K diffusion pump [49] (pumping speed = 3100 L/sec, working pressure < 0.4 Torr, ultimate vacuum less than 3×10^{-8} Torr), which is backed by a RUVAC WA251 roots pump [50] (volume flow rate: 253 m^3/h, max differential pressure = 80 mbar) and a rotary vane pump. A Pirani gauge monitors the diffusion pump backing pressure, and a ballast volume is provided to slow the increase in this pressure, if the backing pump failed [51].

The load-lock is pumped by a TMH 261 turbomolecular drag pump [52] (water cooled, nominal rotation speed = 60000 cycles/min, attainable final pressure < 3.75×10^{-10} Torr) which is connected to a rotary vane vacuum pump.

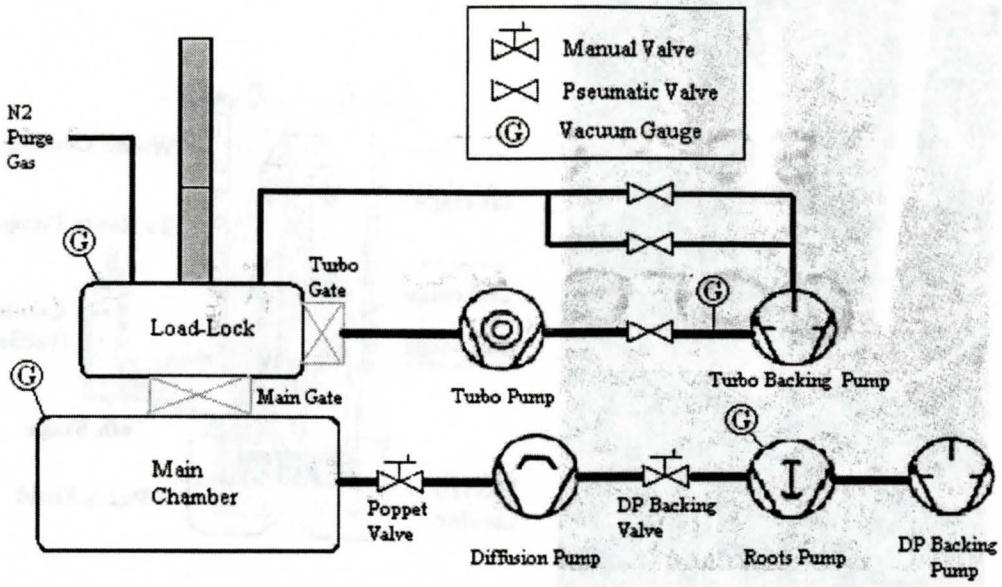

Fig. 3.7 Schematic of the vacuum system used in the ICP-CVD system

In the vacuum system, the diffusion pump is the most important one, because it has to evacuate the main chamber of a big volume to a very low base pressure (10^{-8} Torr) prior to deposition and remove all the active gases at a high speed out of the chamber during deposition. Meanwhile, it is the most complicated one as well and involves most concerns and carefulness in operation when one starts or shuts down the whole system. Therefore, I think it is useful to introduce the basic operational principles of this diffusion pump.

3.2.2.2 Diffusion Pump

Fig. 3.8 (a) presents a photo of the EO9K diffusion pump currently used in the ICPCVD system. The operational principle of this diffusion pump is illustrated in Fig.3.8 (b) [53,54].

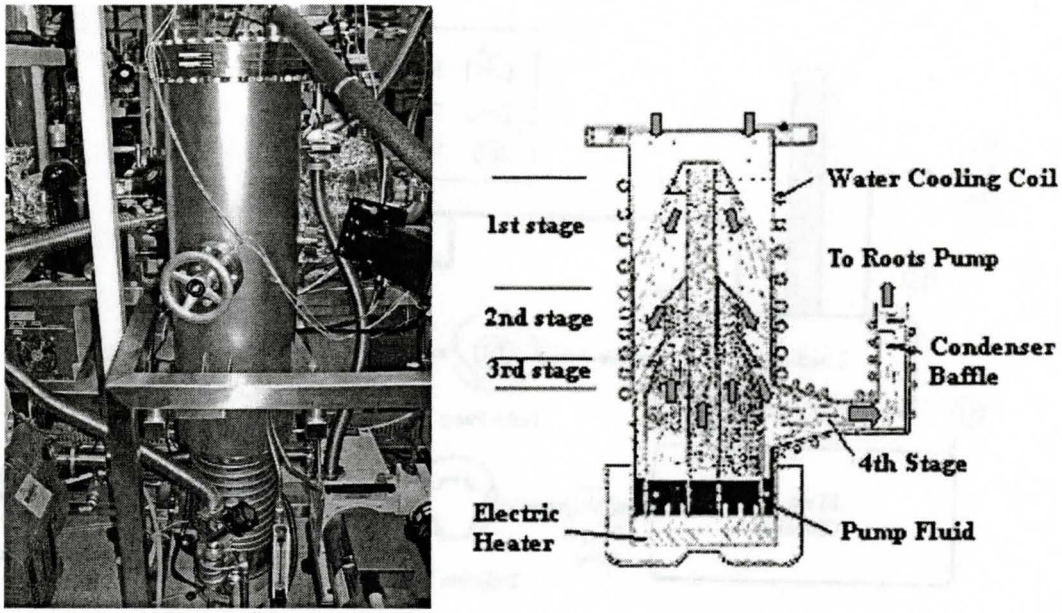

Fig.3.8 The diffusion pump used in the ICP-CVD system (a) the EO9K diffusion pump. (b) Working principle of the diffusion pump

The arrows in the figure show the flow of vapour through the pump. First of all, diffusion pump oil is heated in the boiler at the bottom to produce a vapour that passes up through the interior of the jet assembly and emerges from the pump jets as high-velocity vapour streams. The vapour molecules then collide with the randomly moving gas molecules from above. Because the vapour molecules are generally much more massive than those of the gases being pumped, they can sweep the gas molecules in a downward direction. They then condense on the cold pump body wall, which is cooled by water that flows through a copper tube wound around the pump body, and then drain by gravity into the boiler at the bottom of the pump for re-circulation.

A portion of system gases, which arrive at the pump-inlet, is trapped in the vapour stream from the first-stage jet. The gases are compressed and transferred to the next stage. Gases compressed below the third-stage jet are ejected out of the ejector by a horizontal vapor stream. The exit section has condenser baffles to cool down and condense vapours to prevent the pump oil going into the backing pump line. The process is repeated until the gases are removed by the backing pump through the cooled backing condenser.

Diffusion pumps have many advantages such as high pumping efficiency, low noise and vibration, and reliability, but backstreaming is a major concern for all diffusion pumps. By definition, backstreaming is the migration of minute amount of oil that moves in the opposite direction - toward the inlet of the pump and into the reaction chamber. Usually, baffles and traps are used to reduce backstreaming between the diffusion pump and the processing chamber. A baffle is a plumbing component consisting of surfaces, cooled by chilled water, which condenses the oil vapor and allows it to flow back into the pump. A cold trap is placed above the baffle and is cooled by liquid nitrogen. The trap also condenses water vapor and hydrocarbons from the processing chamber and these vapors will be released when the trap is "warmed up". The use of baffles and traps decreases the backstreaming into the process chamber but also decreases the pumping speed of the diffusion pump.

Our system uses a LN2 liquid nitrogen controller to control the auto-filling and transfer of liquid nitrogen to ensure the cold trap works well with the diffusion pump.

3.2.3 Gas Delivery System

Fig.3.9 shows a schematic diagram of the gas delivery system used in the ICP-CVD system.

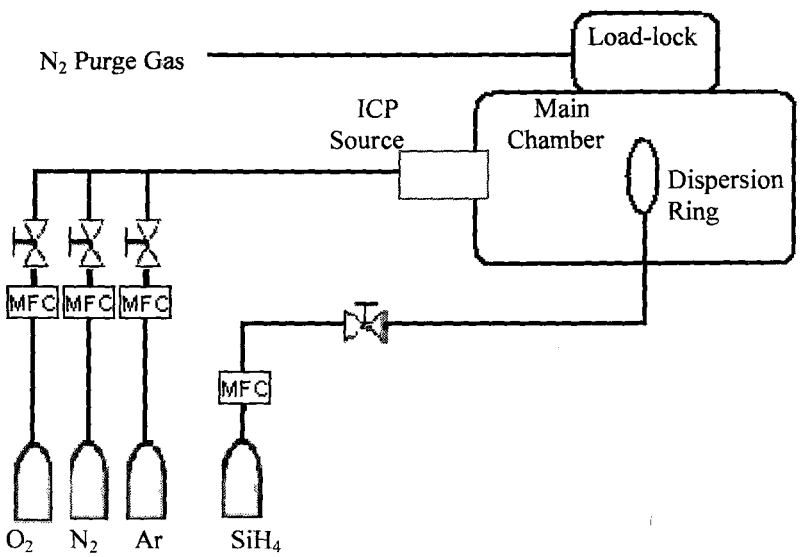

Fig.3.9 Schematic diagram of the gas delivery system in the ICP-CVD system

There are four Matheson SGS® gas cabinets mounted side by side adjacent to the system, which are capable of housing eight gas cylinders in total. Each gas cylinder is connected to ¼" stainless steel tubing via a compressed-gas-distribution system which is composed of a regulator, a variety of valves, and some sensors. For our current system, only six cylinders are in use, providing six kinds of process gases, which are: the O_2 mixture (10% O_2 in Ar), the N_2 mixture

(10% N_2 in Ar), the silane mixture (30% SiH_4 in Ar), pure Ar (UHP grade 99.999%), pure O_2 (UHP grade 99.99%), and pure N_2 (UHP grade 99.999%). Every tubing is connected to the inlet of an 1179A Mass-Flo® controller, and from the flow controller's outlet, to the downstream tubing. The mass flow controller consisting of a positive shutoff valve and a sensor, provides controlling and measuring of the mass flow rate of the gas that flows in the line with an accuracy of ±1% of the full scale reading. After the outlet of the mass flow controller, each of the eight separate gas lines is diverged into two common tubings, with each pathway controlled by an independent valve. Plasma gases, such as O_2, N_2, Ar are introduced from one of the two tubings to the plasma chamber in the ICP source, while silane is fed through the other tubing to the dispersion ring, then into the main chamber.

Silane is an extremely flammable, toxic gas, which can ignite spontaneously or even explode in the presence of air. Therefore, special precautionary measures have been taken in our system for handling and transferring of this pyrophoric gas. An auto-purge dual source controller, model AP220/S_t is mounted in the Semi-Gas System (SGS) - a steel gas cabinet which houses the silane cylinder, to automatically control feeding or cutting off the silane gas. It also provides three sets of programs for changing the cylinder or purging the process gas line, which involve minimal human operations or maintenance, thus virtually eliminating human errors and greatly enhancing the efficiency. For safety consideration, a SM95 sensor transmitter, which is

connected to a MP-202 controller, is placed in the enclosure to detect leaking of silane. Once a silane concentration beyond the set point is detected, the MP-202 will ring an alarm.

Furthermore, a Z1000 Type Z Purge Kit is used to pressurize the SGS controller enclosure with a nitrogen purge gas to minimize the moisture in the enclosure, thus ensuring the electrical circuits inside work in a dry and safe environment.

3.2.4 Temperature Measurement and Control

Although silicon-based dielectric thin films could be deposited at room temperature, a number of researchers have found that, coatings deposited at elevated temperatures seem to be more dense and durable. Hydrogen incorporation can also be reduced. Some other characteristics of the deposited coating, such as refractive indexes and uniformity, are found to be temperature-related. So the substrate temperature is a most important factor in the growth of thin films, and needs to be sensed and controlled accurately.

As mentioned above, the heating mechanism in ICP-CVD uses a resistive coil heater, just like an electric stovetop "burner" in our life, to heat the steel sample holder, which is clasped on the top of the heating stage. The heating process is controlled by a Eurotherm 2404 PID (proportional, integral, differential) temperature controller. The sensor is located below the heater. Since the power applied to the heater is proportional to the difference between the desired set point and the measured temperature, a desired temperature could be quickly achieved

(From 25°C to 300°C takes about 3 minutes) and maintained within an accuracy of ±1°C [55].

Accurate measuring of the substrate temperature is carried out by a retractable thermocouple, which is mounted close to the sample holder. By slowly rotating a knob, the tip of the thermocouple can stretch forth into a slot in the sample holder until it touches the measuring point just below the substrate. Then the substrate temperature can be read on an Omega controller with an accuracy of ±1°C. It should be mentioned that this reading is just an approximation of the real substrate temperature, because the measuring point of the thermocouple is impossible to be imbedded in the surface of the substrate. It is, however, believed to represent the actual substrate temperature very well based on our current measuring technology.

Chapter 4

Ellipsometry

4.1 Introduction

Ellipsometry is a very versatile optical technique, which has been used for about a hundred years to derive information about thin film properties, such as optical constants (n, k), layer thickness, surface and interfacial roughness, composition, optical anisotropy, and crystallinity. The technique is characterized by accuracy, non-destructivity and high-reproducibility. It works by analyzing the change of both the amplitude and phase of a polarized light beam reflected from the sample surface and extracting the sample surface properties (such as film thickness and refractive index) with suitable models.

The measuring technique was first proposed by Paul Drude [55,56] at the end of the 1800's, who used it to determine the dielectric function of various metals and dielectrics. For a long time following Drude's pioneering work, this technique hadn't attracted too much attention of the science and engineering community, until in the late 1960's ellipsometry experienced a renaissance due to the application of computers for high speed data analysis and measuring procedure automation [57]. It has since become one of the most important and powerful tools for the characterization of optical properties, in particular, of thin-film- and multi-layered materials.

4.2 Basic Principles of Ellipsometry

In order to describe light, one usually considers the light wave as an electromagnetic plane wave. The E-field component, B-field component and the direction of propagation of the plane wave are all orthogonal with respect to each other. Because of the relationship between the fields, only the E-field and the direction of propagation are therefore required to define polarization states of light. Light whose electric field oscillates in a particular direction is said to be polarized and the direction in which the E field oscillates is referred to as the polarization of light. Usually, light such as sun-emitted light or a candle flame, is said to be unpolarized light or natural light because it is actually composed of light of all polarizations. Transforming unpolarized light into polarized light can occur in a variety of ways, such as during reflection, refraction, and scattering of light. The polarization of light can be classified into three categories: linear, circular, and elliptical. When the end point of the electric vector of a polarized light beam is viewed along the direction of light propagation, it moves along a straight line if the light is linearly polarized, along a circle if it is circularly polarized, and along an ellipse if it is elliptically polarized.

In ellipsometric experiments it is now common to resolve the E-field of light into E_p and E_s components along the so-called p- and s- directions to express light polarization states, as shown in Fig. 4.1. The plane of incidence is the plane that contains the incident, reflected light and the vector normal to the sample surface. The p-direction is defined as lying in the plane of incidence and

perpendicular to the incident direction. The s-direction lies perpendicular to the p-direction and normal to the plane of incidence.

The states of the two electric field components can be expressed by a Jones Matrix:

$$\begin{bmatrix} E_p \\ E_s \end{bmatrix} = \begin{bmatrix} E_{p0} e^{i\delta_p} \\ E_{s0} e^{i\delta_s} \end{bmatrix} \tag{4.1}$$

Where E_{p0}, E_{s0} are the amplitudes of E_p and E_s respectively, and δ_p and δ_s are phases of E_p and E_s respectively.

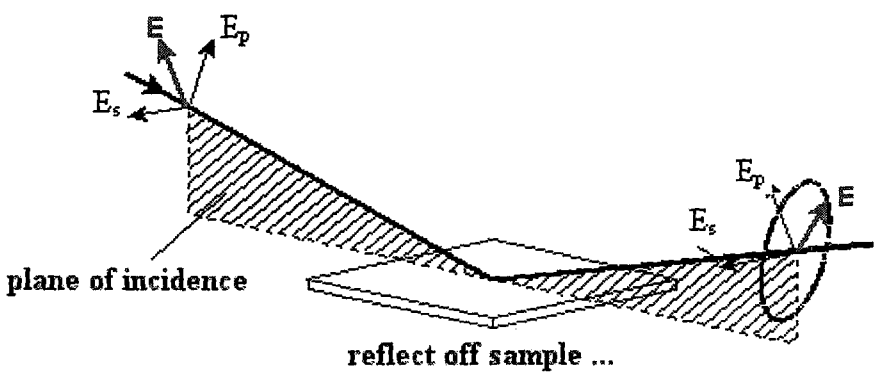

Fig. 4.1 Geometry of an ellipsometric experiment, showing p- and s- directions. Graph taken from [58] and modified a little.

Let us consider the case of a beam of linearly polarized light incident on a dielectric surface. Upon reflection, the two orthogonal components of the E-field of light, E_p E_s, will experience a different attenuation and phase shift, resulting in the reflected light exhibiting an elliptical state of polarization. If we use subscript "in" to represent the status of incidence, "out" to represent the status after

reflection, the reflection process can be depicted by the following reflection matrix R, which connects the incident and reflected E vectors:

$$\begin{bmatrix} E_p^{out} \\ E_s^{out} \end{bmatrix} = \begin{bmatrix} r_p & r_{sp} \\ r_{ps} & r_s \end{bmatrix} \begin{bmatrix} E_p^{in} \\ E_s^{in} \end{bmatrix} \tag{4.2}$$

where r_p , r_s ,r_{sp}, r_{ps} are complex Fresnel coefficients for p and s polarized light, which are defined by the well-known Fresnel equations.

For isotropic materials, where R is diagonal (r_{sp}, r_{ps} = 0), two so-called "ellipsometric angles" ψ and Δ can be defined by the following relations, which are actually measured by the ellipsometer.

$$\rho = \tan(\psi) = \frac{E_p^{out}/E_p^{in}}{E_s^{out}/E_s^{in}} = \frac{r_p}{r_s} = \frac{|r_p|}{|r_s|} e^{i(\delta_p - \delta_s)} \tag{4.3}$$

where ψ and Δ are given by:

$$\tan(\psi) = \frac{|r_p|}{|r_s|} \quad \text{and} \quad \Delta = \delta_p - \delta_s \tag{4.4}$$

Here ρ is defined as the complex reflectance ratio, ψ is an angle whose tangent gives the ratio of amplitude change for the p and s components, corresponding to the amplitude ratio of the reflection coefficients, and Δ denotes the relative phase shift of the p and s components upon reflection. Ellipsometry technology is based on measuring these two angles.

Knowing the ellipsometric angles ψ and Δ, some parameters such as the dielectric function, or pseudo-optical constant ε, and refractive index can be directly obtained by the relation [59,60]:

$$\tilde{\varepsilon} = \varepsilon_1 + i\varepsilon_2 = \sin(\phi)^2 \cdot \left[1 + \tan(\phi)^2 \cdot \left(\frac{1-\rho}{1+\rho}\right)^2\right] \tag{4.5}$$

$$\tilde{n} = n + ik = \sqrt{\tilde{\varepsilon}} = \sqrt{\varepsilon_1 + i\varepsilon_2} \tag{4.6}$$

$$\varepsilon_1 = n^2 - k^2 \tag{4.7}$$

$$\varepsilon_2 = 2nk \tag{4.8}$$

Where ϕ is the angle of incidence. $\tilde{n}$ is called the complex index of refraction, which is a representation of the optical constants of a material. It is composed of a real part n and an imaginary part k. Here n is also called the index of refraction, which is defined as the ratio of the velocity of light in a vacuum to that in a medium. k is the extinction coefficient, which indicates the strength of absorption loss at a particular wavelength. It is related to the absorption coefficient by $k = \frac{\alpha\lambda}{4\pi}$, where α is the absorption coefficient and λ is the wavelength of light.

However, other physical quantities of the film on a substrate under examination, e.g. the thickness, cannot be calculated directly from the ellipsometric angles, because the formulae that describe reflection matrix R as a function of these parameters are complicated and cannot be inverted. Therefore, one has to develop an optical model and fit the output of the model until it best matches the measured values of ψ and Δ. Usually the Root Mean Square Error (MSE) is used to evaluate how good the model fits the experimental data. The expression of MSE is given in (4.9). In general, the smaller the MSE is, the better the model fits the experimental data.

$$MSE = \sqrt{\frac{1}{2N - M}\sum_{i=1}^{N}\left[\left(\frac{\psi_i^{\mathrm{mod}} - \psi_i^{\mathrm{exp}}}{\sigma_{\psi,i}^{\mathrm{exp}}}\right)^2 + \left(\frac{\Delta_i^{\mathrm{mod}} - \Delta_i^{\mathrm{exp}}}{\sigma_{\Delta,i}^{\mathrm{exp}}}\right)^2\right]} \quad (4.9)$$

where $\psi_i^{\mathrm{mod}}, \Delta_i^{\mathrm{mod}}$ are calculated ψ and Δ values based on a particular model. $\psi_i^{\mathrm{exp}}, \Delta_i^{\mathrm{exp}}$ are experimentally measured ψ and Δ values.

Thus the working principle of ellipsometry can be simply summarized as: measure two parameters ψ and Δ, then extract other desired information through a model-based analysis, as shown in Fig. 4.2.

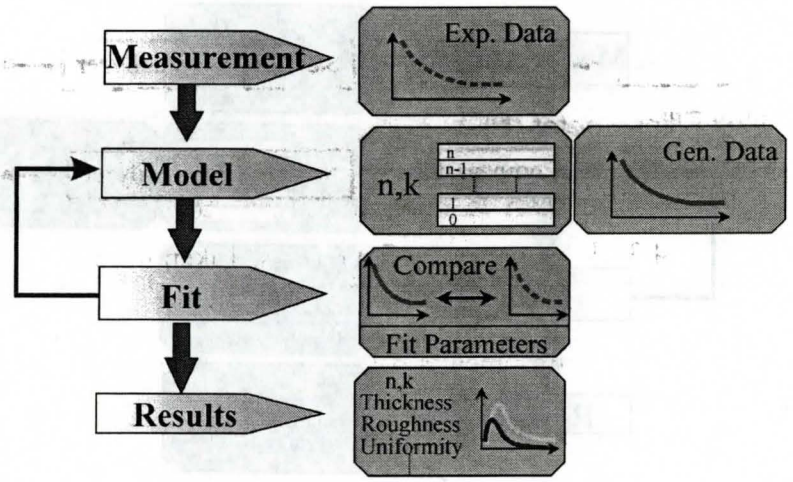

Fig. 4.2 Flow chart of data analysis process in ellipsometry Taken from http://www.jawoollam.com/Tutorial_6.html

4.3 Ellipsometer Configurations

For over a century a variety of different ellipsometer configurations have been developed. As can be seen from Fig. 4.3, there are basically three primary types of ellipsometers null, polarization modulation, and rotating element ellipsometers. It is easy to find that every ellipsometer starts with a light source

and ends with a detector. Two polarizers are placed in between – one on the light source side, the other on the side of the detector.

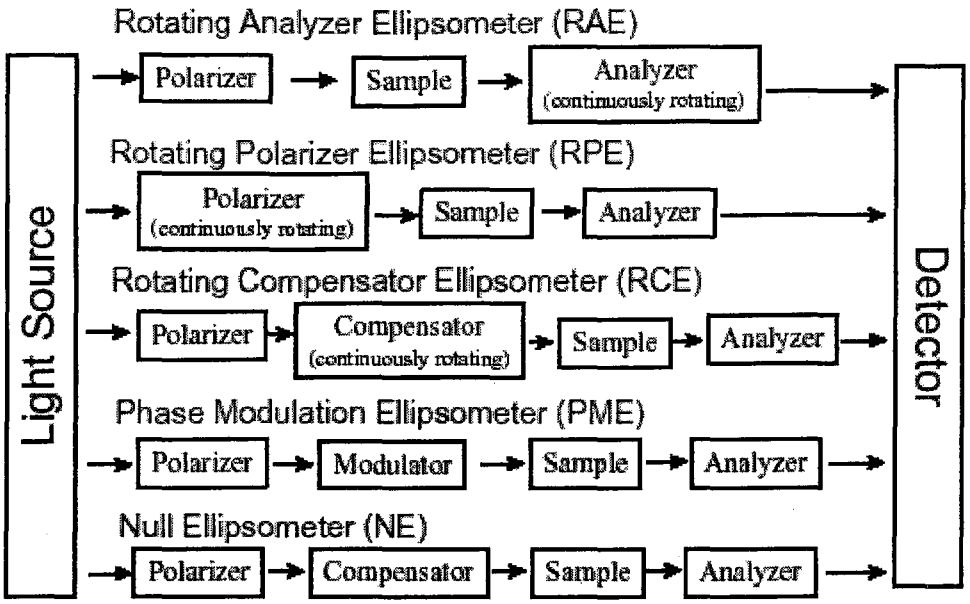

Fig. 4.3 Ellipsometer configurations. Taken from http://www.jawoollam.com/Tutorial_3.html

Historically null ellipsometers were first developed. The basic idea is that, for linearly polarized light, it is possible to extinguish the light incident on the detector by adjusting the orientation of the polarizer, compensator and analyzer. This is called "finding the null". Then ψ and Δ can be measured at this point, which leads to determination of other parameters via proper modelling analysis. So far this method is still used in some single wavelength ellipsometers, just that modern null ellipsometers use computers instead of human hand and eye to adjust the elements and observe the change of signal, and to automatically and quickly calculate the ellipsometry signal. There are several advantages to using this technique and instrumentation to measure the thickness and refractive index of a

thin film. They include high accuracy, high speed, high reproducibility, and the ability to take measurements without a reference sample and low susceptibility to scattering, lamp or purge fluctuations. But it also has some disadvantages, e.g. the amount of information obtained from a sample is limited mainly due to the single wavelength.

Spectroscopic ellipsometry [61 - 63] has become prevalent which employs a broadband light source instead of a single wavelength laser, so sufficient information over a large spectral range could be obtained. Spectroscopic ellipsometers often use the rotating analyzer/detector combination to measure beam polarization states. The input polarizer serves to linearly polarize the beam incident on the sample, and the combination of rotating analyzer and detector allow the measurement of the polarization state of the reflected beam. For a general elliptical polarization the detected signal is a sinusoid with a DC offset of the form (Fig 4.4 [58]):

$$V(t) = DC + a\cos(2\omega t) + b\sin(2\omega t) \qquad (4.10)$$

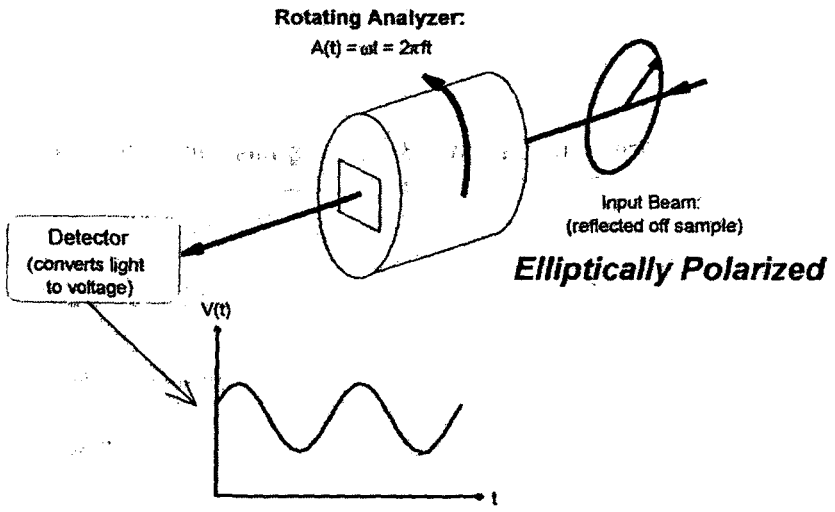

Fig. 4.4 The detector signal associated with an arbitrarily elliptically polarized beam entering the rotating analyzer polarization detector.

The two important quantities measured by the ellipsometer are α and β, which are normalized Fourier coefficients of the signal. They can be represented in terms of the Ψ and Δ values for the sample and the polarizer azimuthal angle P as follows.

$$\alpha = \frac{a}{DC} = \frac{\tan^2 \Psi - \tan^2 P}{\tan^2 \Psi + \tan^2 P} \tag{4.11}$$

$$\beta = \frac{b}{DC} = \frac{2 \tan \Psi \cos \Delta \tan P}{\tan^2 \Psi + \tan^2 P} \tag{4.12}$$

Ψ and Δ are the ellipsometric parameters that characterize the sample, and P is the input polarizer azimuth with respect to the plane of the incidence. The above equations are inverted to obtain Ψ and Δ from the measured α, β and the known P.

The Philips PZ2000 ellipsometer (see Fig. 4.5) used in this project is actually a rotating analyzer ellipsometer (RAE), which works according to the principle introduced above. The schematic setup of the optical components for the PZ2000 ellipsometer is illustrated in Fig. 4.6.

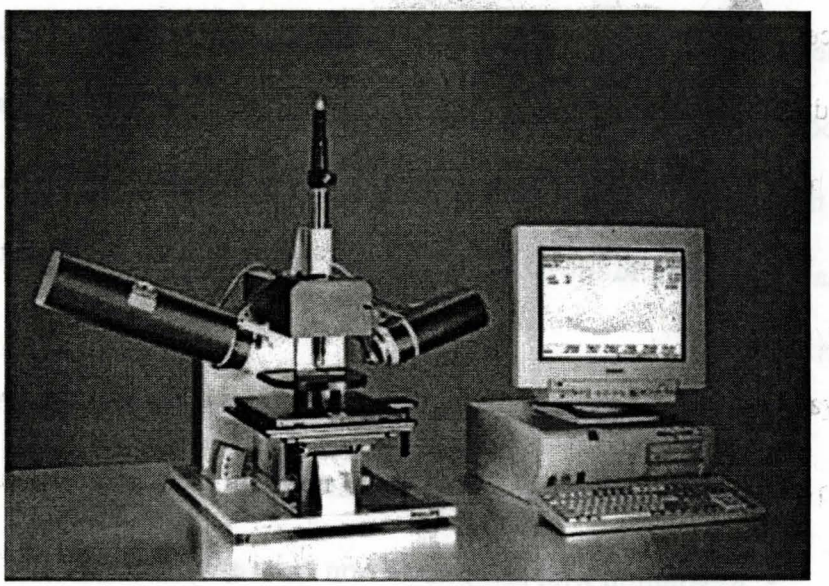

Fig.4.5 Philips PZ2000 laser ellipsometer working at the wavelength of 632.8nm

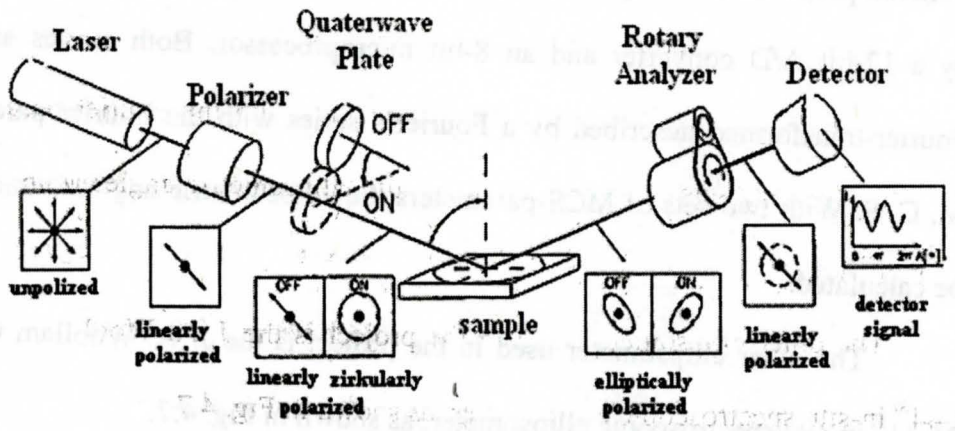

Fig.4.6 Schematic setup of the optical components for the Philips PZ2000 laser ellipsometer [64].

The PZ2000 ellipsometer [64] uses a HeNe laser (wavelength = 632.8 nm) as the light source. During the measurement the polarizer is always fixed at an azimuth of +45°, and the analyzer is rotating at a constant speed.

The light coming from the laser source is directed through a polarizer to produce a linearly polarized beam; then through a compensator (quarterwave plate) to produce polarized light in a circular way. The beam finally comes into contact with the surface of the sample with an incidence angle of 70°. A polarizer in permanent rotation followed by a photo detector makes the analysis of the state of polarization.

Measurement is taken during two revolutions of the polarizer:

- Revolution without compensator
- Revolution with compensator on the way of the beam

The output signal behind the rotating analyser is recorded with the help of a silicon photo diode at high amplification. The sinusoidal output is then digitized by a 12-bit A/D converter and an 8-bit microprocessor. Both curves are then Fourier-transformed described by a Fourier's series with the Fourier parameters M, C, S. With two sets of MCS-parameters the ellipsometric angles ψ and Δ can be calculated.

The other ellipsometer used in the project is the J. A. Woollam Co. Inc. M-44® in-situ spectroscopic ellipsometer, as shown in Fig. 4.7.

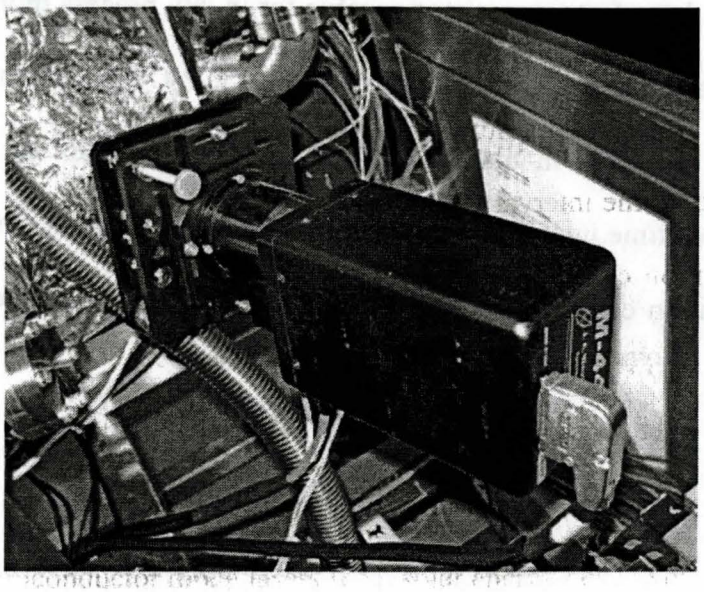

Fig.4.7 The in-situ M-44® ellipsometer mounted on the ICP-CVD system

It is also a rotating analyzer ellipsometer. The basic operational principle is the same as that of the PZ 2000 ellipsometer The difference is that the M-44® ellipsometer uses a broad band light source instead of a single wavelength laser, to shine a white light on the sample surface. The light reflected from the sample through the rotating analyzer is then dispersed off of a grating onto a 44-element diode array, which can simultaneously measure 44 wavelengths from 600 to 1100 nm. Because the detectors of the M-44® ellipsometer correspond to fixed wavelengths, it is much easier to calibrate than it is for a standard scanning monochromator with a continuous wavelength range (A scanning monochromator with a moving grating does not permit simultaneous measurements at multiple wavelengths.). The M-44® ellipsometer also does not require any collecting optics (lenses). The probe beam directly enters the detector unit and does not need to be

focused. All these features make it suitable for in-situ process monitoring, where rapid data acquisition is necessary. In the ICP-CVD system, the M-44® ellipsometer measures in-situ thickness and refractive index of deposited thin films at a fixed time interval during the deposition and sends the measured results to the deposition control computer. Thus, automatic multilayer deposition could be achieved.

Chapter 5

Deposition of Silicon-Based Dielectrics by Inductively Coupled Plasma Chemical Vapor Deposition

5.1 Introduction

Silicon-based dielectrics have long found widespread applications as gate insulator and passivation layers for elemental and compound semiconductor device structures, anti-reflection and highly reflective optical coatings, facet coatings for semiconductor diode lasers [65], solar energy cells, Xerography, thin-film transistors for active-matrix liquid crystal displays and ICs [4]. Silicon-based dielectrics, which are currently used in semiconductor industries, are mainly silicon oxide, silicon nitride and silicon oxynitride.

Among different approaches that have been developed to produce these dielectric films, plasma-enhanced chemical vapor deposition (PECVD) is one of the most important and efficient methods.

There are primarily three types of PECVD: conventional PECVD, remote PECVD, and HDP-PECVD. In conventional PECVD, the substrate is located in the plasma zone. As a result, the substrate is subject to energetic particle bombardment, which may damage the wafer. Also, since all of the feedstock gases are flowed through the plasma, one has little control over the reaction pathways. Remote PECVD differs from conventional PECVD in that the substrate is not in direct contact with the plasma and thus is not subjected to ion

bombardment. Since the deposition gases are not flowed through the plasma zone, a greater degree of control over production of radicals is also possible.

Recently, high density plasma CVD (HDP-CVD) has increasingly been used for thin film deposition. The HDP-CVD uses either electron cyclotron resonance (ECR) or inductively coupled plasma (ICP) sources for high-density plasma generation. Compared to those produced by the conventional plasma CVD process, dielectric films deposited by HDP-CVD have not only better gap-fill properties but also improved physical, chemical, and electrical properties [4].

5.2 Preparation of SiO_x Films by ICP-CVD

5.2.1 Sample Preparation

In this project, single-side polished, two-inch, (100) Si wafers (undoped) were used as substrates. Silicon oxide, silicon nitride, and silicon oxynitride thin films were deposited by ICP-CVD. Prior to deposition, all the samples were thoroughly cleaned in the McMaster Clean Room. The wafers were treated sequentially in ultraviolet (UV) zone, buffered HF ($HF:H_2O$ = 1:10) and de-ionized (DI) water to effectively remove inorganic/organic contaminants from the sample surfaces. The whole cleaning procedure consisted of the following steps:

1. Buffered HF for 3 minutes
2. Rinse in flowing DI water for 10 minutes
3. Blow dry
4. UV ozone for 20 minutes
5. Buffered HF for 5 seconds

6. DI rinse for 10 minutes
7. Blow dry

5.2.2 System Maintenance

Prior to every deposition, a UHV (usually on the order of 10^{-8} Torr) base pressure environment in the processing chamber must be maintained to reduce the contamination contribution of the vacuum environment during deposition. However, when depositing a material on wafers, it also deposits on the walls of the chamber. During deposition, these residues could be ejected from the chamber wall by ion bombardment and incorporate into the deposited film. P. Mascher and J. Wojcik [66] found that, after thorough chamber cleaning, the hydrogen concentration in ECR-CVD-fabricated silicon oxynitride thin films could be reduced to half of the previous level (see Fig. 5.1).

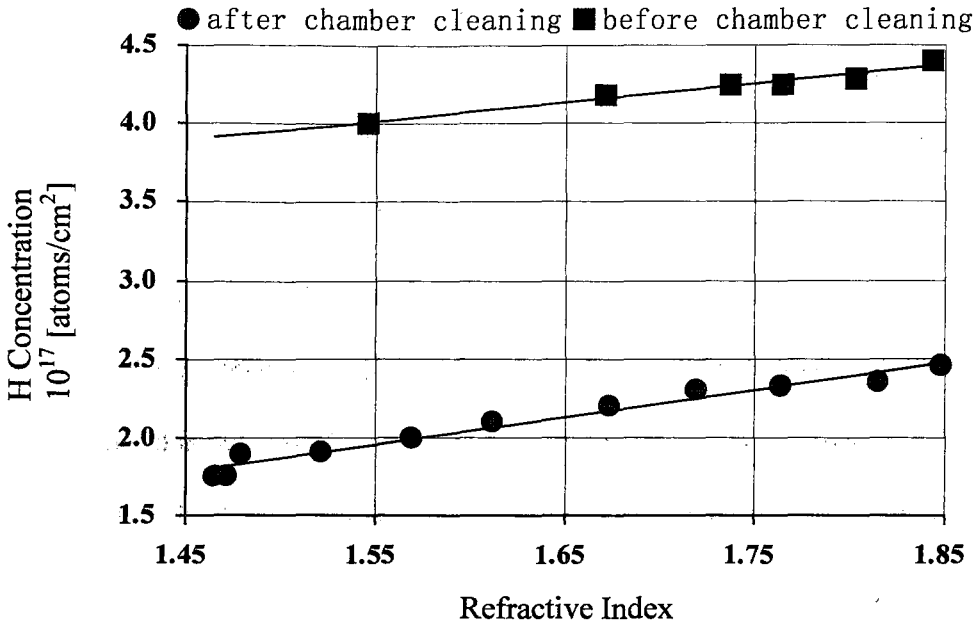

Fig. 5.1 Hydrogen concentration determined by ERD in SiO_xN_y thin films before and after thorough chamber cleaning. Taken from [66], modified a little.

So, prior to the first time using of the ICP-CVD system or starting a new deposition using different reactant gases, the processing chamber must be baked at 150°C for 24 hours, and then "cleaned" by an Ar plasma at 700W for 20 minutes to remove any possible residues and annihilate the "chamber history" effect. "Baking out the chamber" actually means heating up the walls and outgassing deposited materials on the walls. Similarly, high-energy electrons and Ar ions in the Ar plasma can also sputter the deposited species off of the chamber wall, which are then removed by the diffusion pump. Both methods help to prevent contamination in the process.

5.2.3 Sample Loading and Film Deposition

After cleaning, the substrate was placed on a round 2-inch sample holder and then clipped tightly on the surface of the holder. Blowing the wafer surface with dry nitrogen gas to remove any possible dust or vapor, the holder was protected by a glass cover and carefully placed into the load-lock. When the load-lock was pumped down by a turbo pump to a pressure less than 6×10^{-7} Torr, a main gate valve between the load-lock and the main chamber was opened, and the sample holder was carefully transferred into the main chamber via a transferring manipulator. It took about 15 minutes from pumping the load-lock to placing the sample holder in position onto the top of a stage heater. Then the main gate valve was closed, and the main chamber was evacuated to a base pressure below 10^{-8} Torr.

Once in the chamber, the sample temperature was raised to a desired temperature by the stage heater underneath the sample holder, and left to outgas until the main chamber base pressure was below 9×10^{-8} Torr.

Because my project is to find out optimal conditions for depositing silicon oxide thin films with excellent uniformity and desired optical characteristics, a number of depositions were done under various conditions. Exact deposition conditions will be given in Chapter 6 of this thesis. After deposition, the samples were allowed to cool down to room temperature, and then were removed from the system.

5.3 Deposition Chemistry of Silicon Oxide Thin Films

5.3.1 Reaction Mechanisms

In ICP-CVD, energy from the external RF source is coupled into the reactant gases, generating a lot of reactive species. Collisions among these species give rise to reactions and depositions on substrate surfaces. Thus, it is fundamental to investigate the reaction mechanisms during plasma deposition.

We know that in the gas phase environment of a plasma, there exist electrons, ions, neutral atoms and molecules, and photons. The collisions between all possible pair permutations can be broadly divided into elastic and inelastic types. Particles usually have two types of energy: kinetic energy due to their motion and equal to $\frac{1}{2}mv^2$ for translational motion, and internal or potential energy with may be in the form of electronic excitation or ionization. In the elastic collisions, only minimal translational energy transfer occurs between the gas molecules and reactant gases. For plasma processing, the elastic collisions play a less important role in reactant dissociation [4]. All other types of collisions are inelastic, which mainly include collisions involving electrons, ion-neutral collisions, and metastable collisions.

There are primarily six types of inelastic electron-involving collisions, which include:

- Electron impact ionization: the most important form of inelastic electron collisions, in which the primary electron removes an electron from the atom, producing a positive ion and two electrons, e.g.

$$e + Ar \rightarrow 2e + Ar^{+} \tag{5.1}$$

The two electrons produced by the ionizing collision can then be accelerated by an electric field until they, too, can produce ionization. It is by this multiplication process that a plasma is maintained.

- Recombination: the inverse of ionization, in which an electron coalesces with a positive ion to form a neutral atom.
- Excitation: the collision between an electron and an atom just causes an electron to jump to a high level within the atom, rather than to be ejected from that atom, e.g.

$$e + Ar \rightarrow Ar^{*} + e \tag{5.2}$$

- Relaxation: the inverse of the excitation process. The electron at excited states is unstable and soon returns to its original state, accompanied by the emission of a photon.
- Dissociation: the process of dissociation is the breaking apart of a molecule, e.g. $e + O_2 \rightarrow e + O + O$ (5.3)
- Electron-metastable ionization: Just as a ground state atom can be ionized by electron impact, so can a metastable:

$$e + Ar^{*} \rightarrow Ar^{+} + e + e \tag{5.4}$$

Besides electron collisions, ions and neutrals can collide with each other inelastically or elastically to either exchange charges or cause further ionization.

Some excited atoms have very long lifetimes, and are known as metastable excited atoms. Metastable collisions could take place between a metastable atom and a neutral, e.g.

$$Ar^{\bullet} + O \rightarrow O^{+} + Ar + e \tag{5.5}$$

This is known as Penning ionization.

Also, two metastable atoms can collide with each other and result in the ionization, e.g.

$$Ar^{\bullet} + Ar^{\bullet} \rightarrow Ar + Ar^{+} + e \tag{5.6}$$

We have now reached the state where we can begin to consider reaction mechanisms in the ICP-CVD process. Though the exact reactions during plasma deposition are complex and not completely understood (elementary reactions that occur in a plasma have been discussed by various authors [67 - 70]), a very high-level discussion on this issue can still be given as below:

When the plasma initiates, energy from the RF electric field is coupled into the reactant gases via the kinetic energy of a few free electrons. These electrons gain energy rapidly through the electric field and lose energy slowly through elastic collisions. The high-energy electrons are capable of inelastic collisions that cause the reactant gas molecules to dissociate and ionize, producing secondary electrons by various electron-impact reactions, and finally a steady-state plasma is sustained in the processing chamber. The plasma discharge

contains a lot of radical and ion reactive species. When the flux of these reactive species reaches and strikes the surface of the film being deposited, various gas-phase chemical reactions take place there. The bombardment by the ionic species of the surface of the film controls the surface mobility of the precursor, and is the predominant factor in determining film composition, density, and stress.

Some of the inelastic collisions between inert gases and reactants (such as argon with silane) significantly affect the chemical nature of the discharge and the properties of the deposited films. In our ICP-CVD process, an inert carrier gas (Ar) is used to dilute O_2 or N_2, so as to form a "cooler" plasma, and to create more controlled reaction pathways via Penning reactions between carrier and reactant gases.

5.3.2 Deposition Mechanism

In general, the ICP-CVD process is a four-step process [4,68] in which the films are deposited outside of the plasma region. The four steps could be qualitatively described as follows:

1 The RF excitation of a gas, or gas mixture that contains molecules with either oxygen or nitrogen to form ions and radical reactive species through electron-impact reaction.

2 Transport of these reactive species (such as excited oxygen or nitrogen species and other atoms, molecules, radicals, and electrons) out of the plasma region

3 The mixing and gas phase reaction of the excited species with neutral silane, to generate gas phase deposition precursors;

4 A CVD reaction on the surface of a heated substrate, this step actually includes two aspects: on the one hand is the reaction and/or incorporation of deposition precursors, at the same time, the reactive species that have been deposited on the substrate could re-emit back to the gas phase.

For our current project, a mixture of $SiH_4/O_2/Ar$ was used to obtain SiO_2. The net reaction can be described by the following equation:

$$(O_2, Ar) + SiH_4 \rightarrow SiO_2 + Ar \tag{5.7}$$

In step 1, the O_2/Ar mixture excited by the inductively coupled plasma is, mainly through electron-impact process, decomposed into active species, which include oxygen atoms, excited Ar atoms, electrons and some oxygen and argon ions (O_2^+, O^+, Ar^+). Kushner and co-workers' experiments [71] confirmed that the dominant ions that exist in the mixture of Ar/O_2 in the plasma zone is O_2^+, which is produced primarily by electron impact and secondarily by Penning ionization by Ar^*. O^+ and Ar^+ are produced in approximately the same density, with the former primarily being produced by charge exchange from Ar^+ to O_2. The possible processes are suggested as below [68,71]:

$$Ar^* + O_2 \rightarrow O_2^+ + Ar + e \tag{5.8}$$

$$Ar^+ + O_2 \rightarrow O_2^+ + Ar \rightarrow O^+ + O + Ar \tag{5.9}$$

Next, in step 2, these excited species diffuse from the plasma zone through an aperture pattern into the main chamber.

Step 3 is characterized by neutral reaction chemistry [71]. This is because in this step, the vast majority of the species transported out of the plasma regime are neutral. The various species are then mixed with the silane gas, which is introduced into the chamber from a dispersion ring in the middle of the main chamber. This mixing can lead to the formation of gas phase precursors that contain the structral building block of the deposited thin film. For example, the reactions of O atoms with neutral SiH_4 molecules could produce various possible precursors such as SiH_3 , SiH_2O, HSiO, SiO, SiH_3O and SiH_2O_2. The reaction chemistry is so complex that, to our knowledge, the final precursors which are fomed in the process are still not quite certain. The experiments of Kushner and co-workers [71] suggested that SiH_2O, SiH_3O and SiH_3 are three most likely gas-phase precursors because they found in their experiments that the fluxes of these three species were sufficient to account for the observed deposition rates. The studies of Longeway *et al.* [70] suggested one of the most important precursors produced in this step is disiloxane, $(SiH_3)_2O$, which contains the planar Si-O-Si group-a typical structural building block for stoichiometric SiO_2. A detailed list of possible reactions and the rate coefficients for each reaction in conditions of low deposition pressure is given in [71].

Finally in step 4, all the species, particularly the precursors, reach the surface of the substrate heated by a stage heater underneath. Then a series of sophisticated chemical reactions happen on the surface, resulting in the formation of silicon oxide films. Lucovsky [68] believed that the surface CVD reactions are

mainly the elimination of H from the SiH_3 groups of disiloxane via a reaction in which the terminal H atoms are replaced by bridging O atoms, while M. K. Kushner [71] suggests that surface-catalyzed reactions between O and SiH_n are the main reason to form the final SiO_2 thin films. But none of their arguments are in conflict with what Tsu [72] and Thiel *et al.* [73] showed in their reports that the net reactions leading to film growth are

either $SiH_4 + O_2 \rightarrow SiO_2 + 2H_2$ (5.10)

or $SiH_4 + 2O_2 \rightarrow SiO_2 + 2H_2O$ (5.11)

depending on the gas flow ratio of O_2 and SiH_4.

Chapter 6

System Calibration

6.1 Introduction

The ICP-CVD system is designed to be capable of producing single or multiple layers of thin films, the thickness of which could be precisely controlled within a wide range from tens of angstroms to several micrometers. As described in Chapter 3, our ICP-CVD system is a complicated system, as many factors such as temperature, chamber pressure, gas flow rate, RF power, and plasma density could play different but important roles in thin film depositions. To study the optimal conditions for silicon oxide thin film deposition in this ICP-CVD system, my work primarily includes the following four aspects: temperature calibration, minimum reflected power, optimal uniformity, and refractive index calibration.

6.2 Temperature Calibration

In the ICP-CVD system, the substrate is heated by a resistive heater, which is controlled by a Eurotherm® 2404 PID (proportional, integral, derivative) controller. But the temperature we read from the controller just reflects the temperature of the heater. Since the sample is placed on the surface of a metallic sample holder mounted on the top of the heater, the heater temperature is different from that on the sample holder's surface due to thermal resistance. To measure the temperature of the substrate, a retractable thermocouple that can stretch out to

contact the sample holder, is used in our ICP-CVD system. But because the stage heater will be rotated during the deposition process, an in-situ measurement of the substrate temperature cannot be carried out once the deposition starts. In order to precisely control the substrate temperature during deposition, we need to know how the temperature of the heater, which is reflected by the PID controller, is related to the temperature of the substrate, which is reflected by an Omega CN76000 controller. Once the conversion relation is known, a precise controlling of the substrate temperature is available during deposition, without compromising the deposition process.

In the course of experiments, five groups of data were collected in a temperature range of 200 ~ 400°C, three of which were measured from low to high temperatures, the other two in a sequence of decreasing temperatures. Results are shown in Fig. 6.1. A linear fit, as presented by the red line, revealed an empirical relationship between the temperature of the stage heater and that of the substrate as below:

$$T_{substrate} = 0.3303 \times T_{stage\ heater} + 21.58\ (°C) \qquad (6.1)$$

As an example, some of the experiments were done at a temperature of 300°C, which implies the actual substrate temperature is just 121 ±1°C.

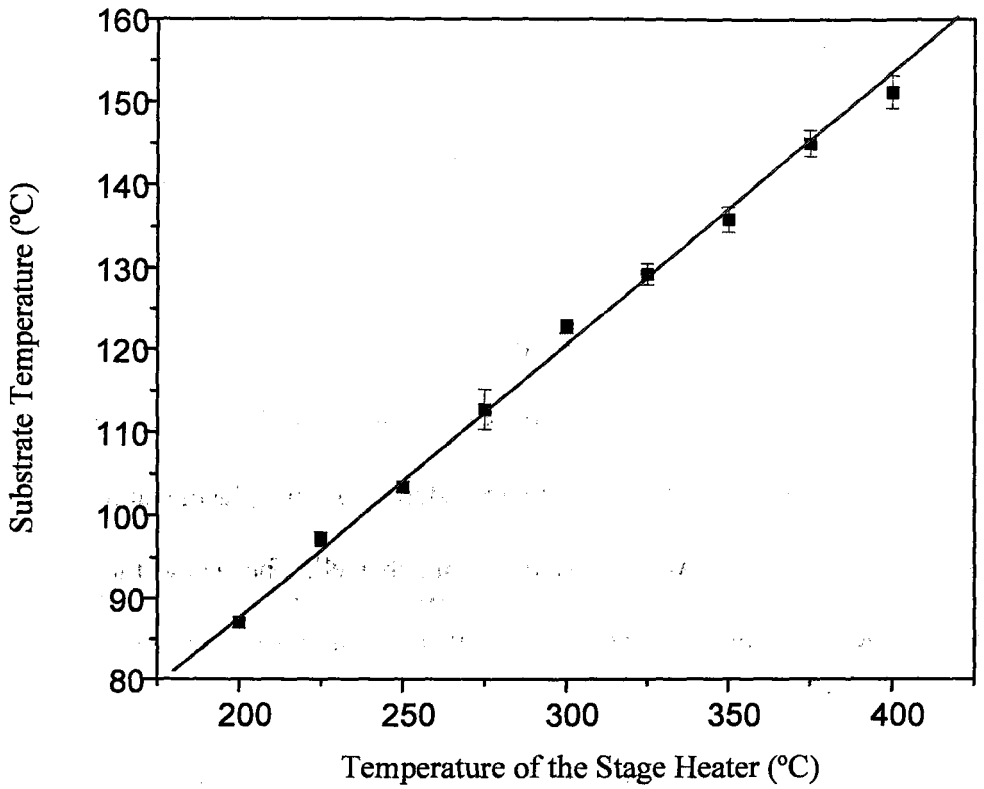

Fig. 6.1 Temperature calibrations – the substrate temperature vs. the temperature of the stage heater

6.3 Minimum Reflected Power Calibration for Different Gases

All the gas flows are controlled by an MKS647B 8-channel gas flow programmer. Plasma gases, such as N_2, O_2, and Ar are introduced through a common process gas line via a plasma gun into the main chamber. Precursor gases, such as SiH_4, are fed to the main chamber from a dispersion ring via a separate channel. As introduced in Chapter 3, the ICP-CVD system uses an ICP source to generate a high-density plasma. The ICP source, sometimes called the

plasma gun, is mainly composed of a PBN tube surrounded by a solenoidal copper coil. Periphery equipment includes a ROBO RFXII 3000 power source, a plasma controller, and a matching system. The power source is capable of generating a 13.56 MHz radio frequency (RF) with a wide range of power from 0 to 3000W. The RF currents flowing in the induction coil can induce a time-varying magnetic field, which subsequently generates an azimuthal electric field, and finally resulting in the formation of a plasma. Via the induced electric field, a large portion of power that the RF carries is coupled into the plasma, and the other portion will be reflected back if the impedance of the plasma and the output impedance of the RF power supply don't match well. The worse the impedance match is, the larger the reflected power will be. It may overheat the components or even result in quenching of the plasma if the reflected power dissipating in the chamber and circuits exceeds a certain amount. In our system, a matching network is used to help match the impedance of the plasma to the output impedance of the RF power supply. In addition to the series capacitor, there is a shunt adjustable capacitor to ground in the matching box. A control circuit within the matchbox controller senses the reflected power (from the matchbox and plasma back to the power supply) and adjusts the variable capacitor to minimize the reflected power. Usually this is done automatically by means of reversible motor drives on the capacitor, but the tuning network can also be manually controlled for special cases.

In this work, we explored the ignition of plasmas from five kinds of gases at different flow rates, varied form 1 to 90sccm. The gases are, pure O_2 (99.99%), pure N_2 (99.999%), a nitrogen mixture (10% N_2, 90% Ar), an oxygen mixture (10% O_2, 90% Ar), and pure Ar (99.999%). For every gas flow rate, the forward power was varied from 200 to 400W, with an increment of 20W Once the plasma was ignited at each forward power, the reflected power was carefully tuned to minimum. Shown below are some of the results.

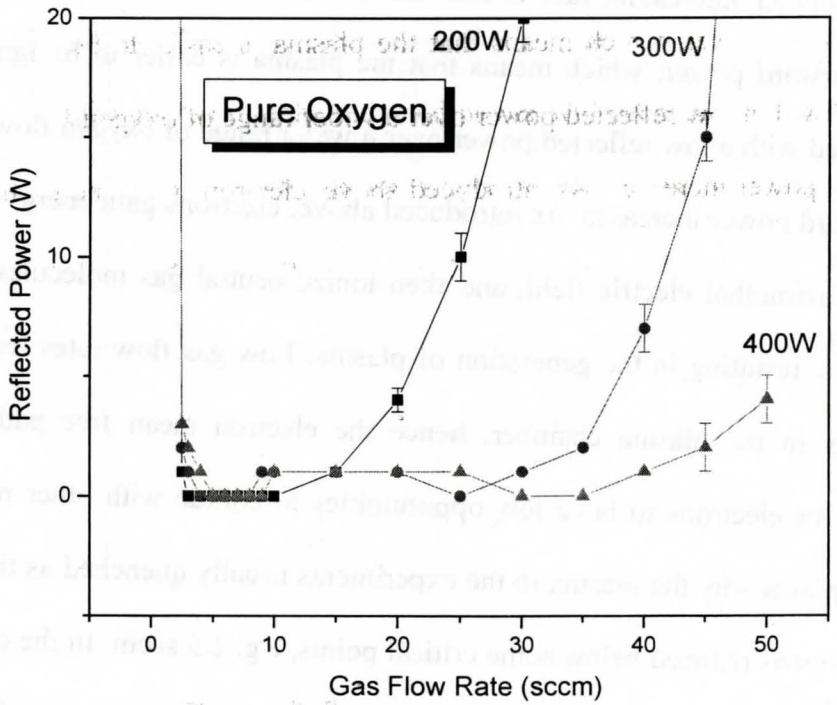

Fig. 6.2 Reflected power calibration as a function of gas flow rate for pure oxygen.

Fig. 6.2 shows the minimum reflected power as a function of pure oxygen flow rate with forward powers of 200W, 300W and 400W respectively. We

observed that, at either low or high oxygen flow rates, the minimum reflected power is bigger than at a flow rate in between. When the flow rate drops below 2.5sccm, the plasma extinguishes. As the oxygen flow rate varies between 3 and 10sccm, the reflected power can be tuned to zero, if the case of forward power of 200W (see the curve in black color in Fig. 6.2) is considered. Beyond the point of 10 sccm, the minimum reflected power increases quickly with the oxygen flow rate.

Another interesting fact is that the curve shows a wider flat bottom at higher forward power, which means that the plasma is easier to be ignited and maintained with a low reflected power over a wider range of oxygen flow rates as the forward power increases. As introduced above, electrons gain energy from the induced azimuthal electric field, and then ionize neutral gas molecules through collisions, resulting in the generation of plasma. Low gas flow rates lead to low pressures in the plasma chamber; hence the electron mean free path is long enough for electrons to have few opportunities to collide with other molecules. This explains why the plasma in the experiments usually quenched as the oxygen flow rate was reduced below some critical points, e.g. 2.5 sccm. In the case of the other extreme, where the gas flow rate is too high at high pressure, and the mean free path is shorter, electrons experience some weak collisions if the energy coupled from the RF source is not high enough. In this case some forward energy coupled into the plasma is wasted in the weak collisions. This scenario is proved by the experimental results: the reflected power initially remains constant over a

range of gas flow rates, and then increases with the gas flow rate if it is further increased. So in most cases, the dependence of the reflected power on the gas flow rate demonstrates a "U-shape" behavior.

Let us consider another situation that, at a given forward power, say 200W, the reflected power starts to increase as the oxygen flow rate is above 15 sccm, due to some "non-effective collisions" mentioned above. The fundamental reason behind this is that many electrons cannot obtain enough energy from the induced electric field. If, at this moment, we increase the forward power to a higher level, say 400W, those electrons will then gain enough energy to undergo "effective collisions" so that the reflected power will decrease. When the oxygen flow rate is increased to such a point, where the mean free path is so short that electrons have no time to obtain enough energy from the induced electric field due to too frequent collisions, the "non-effective" collisions gradually become dominant, which will again cause the reflected power to increase with the gas flow rate. From Fig. 6.2, we can see clearly that the 300W-curve has a wider bottom than 200W-curve, and 400W-curve shows a much wider flat bottom than the other two.

Shown in Fig. 6.3 is the plot of minimum reflected power vs. flow rate of Ar-diluted oxygen at forward powers of 200, 300 and 400W, respectively. A smooth tail in Fig. 6.3 instead of an upswept one in the high-flow-rate section implies that a small reflected power could be obtained even though the oxygen flow rate is very high. This change is attributed to the addition of argon.

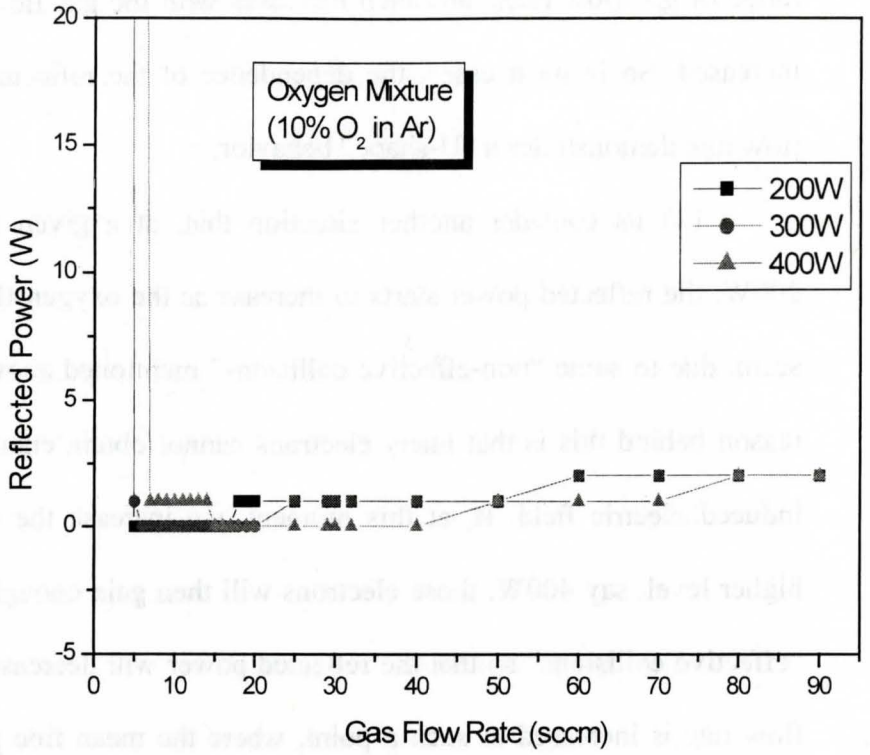

Fig. 6.3 Reflected power calibration as a function of gas flow rate for an oxygen mixture (10% O_2 in Ar).

Since atoms of noble gases, such as Ar, are easy to be excited to metastable electronic states, with considerable radiative lifetimes, the addition of argon to oxygen passing through the discharge region leads to a significant increase in the atomic oxygen concentration because of selective excitation of the molecular oxygen by argon atoms in metastable states [74] Therefore, the plasma of argon-diluted oxygen is easier to be ignited and sustained. As can be seen in Fig. 6.4, the minimum reflected power is not sensitive to the argon flow rate. Even when we increased the gas flow rate to as high as 90 sccm, the reflected power could still be tuned to 0W

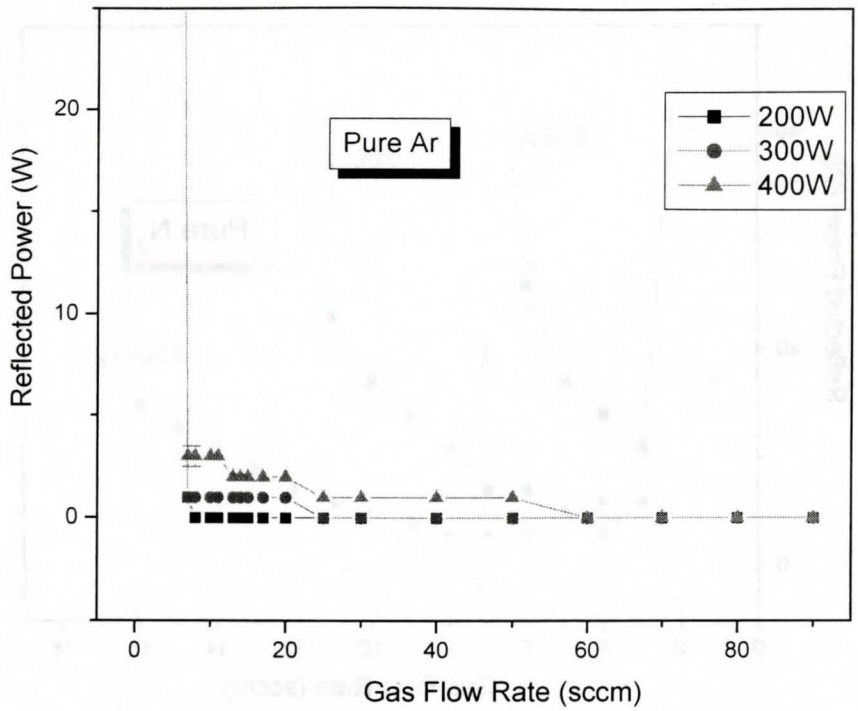

Fig. 6.4 Reflected power calibration as a function of gas flow rate for pure argon.

Figures 6.5 and 6.6 present the reflected power calibration as a function of gas flow rate for pure nitrogen and a nitrogen mixture (10% N_2 in Ar), respectively They demonstrate similar curve shapes and trends as pure O_2 in Fig. 6.2 and the O_2 mixture in Fig. 6.3, respectively So a similar discussion can be applied to Figures 6.5 & 6.6, which will not be repeated here. Generally speaking, the ICP is not too sensitive to the gas flow rate. From observation, the ICP tends to be created at a lower gas flow rate, and maintained at a lower reflected power, compared with the ECR plasma.

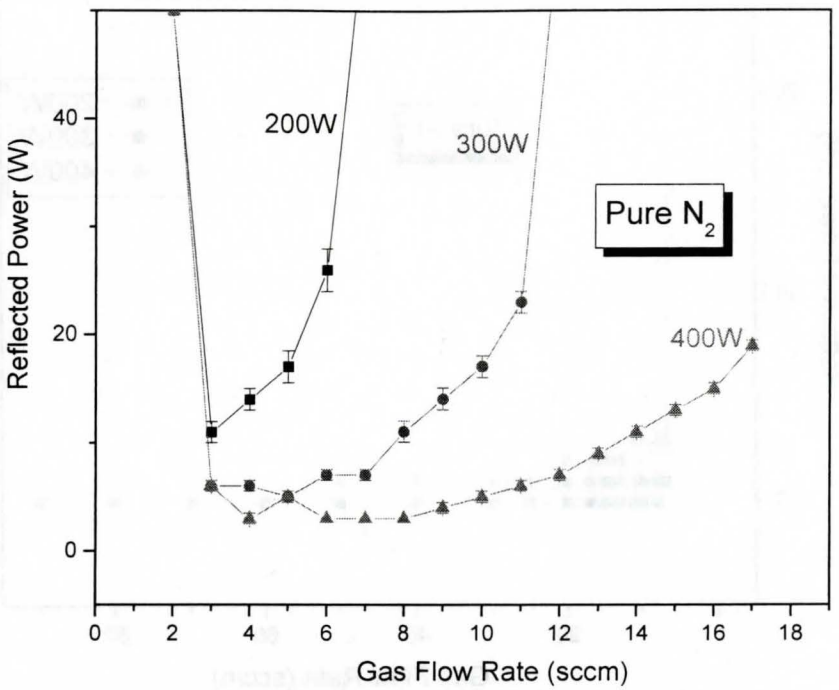

Fig. 6.5 Reflected power calibration as a function of gas flow rate for pure nitrogen.

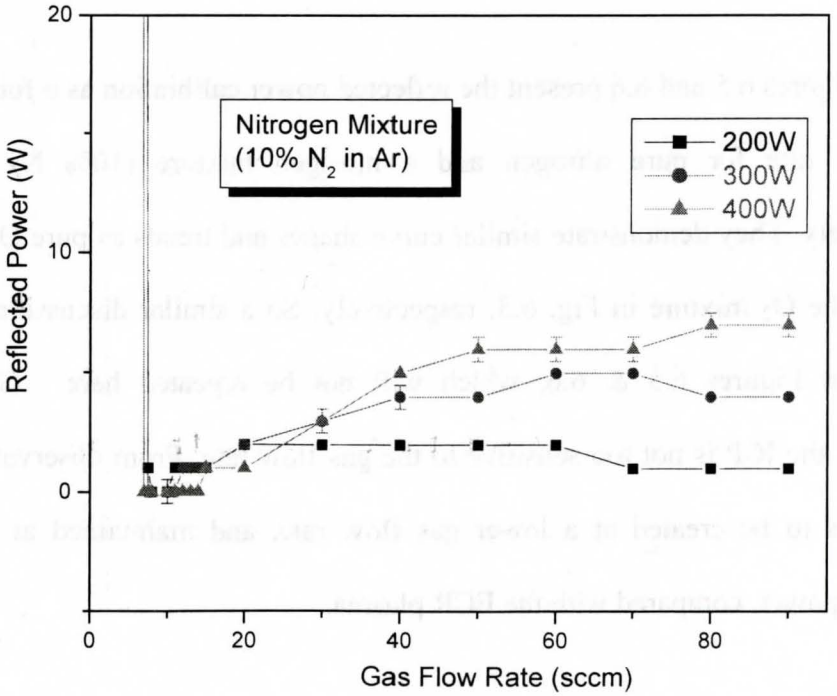

Fig. 6.6 Reflected power calibration as a function of gas flow rate for a nitrogen mixture (10% N_2 in Ar).

6.4 Uniformity Calibration

The uniformity of thickness and surface roughness are the most important parameters to evaluate the quality of CVD deposited thin films, since they directly affect the optical and electrical properties of the deposited thin films. Moreover, the uniformity of thickness within the whole layer is of crucial importance for production, since many interfacial properties are controlled by surface structure. In this project, the uniformity of thickness across the wafer is defined as the standard deviation of the mean thickness of the deposited layer and is expressed as a percentage of mean thickness, as shown below:

$$Uniformity = \frac{\sqrt{\frac{1}{N-1}\sum_{i=1}^{N}\left(X_i - \overline{X}\right)^2}}{\overline{X}} \times 100\,\% \qquad (6.2)$$

Where $\overline{X}$ is the mean thickness, X_i is the measured thickness at measuring point i, and N is the total number of points where measurements have been taken.

For the optimization of the uniformity of thickness across the whole wafer, single layers of silicon oxide thin film were deposited on 2-inch silicon wafers by ICP-CVD under various conditions. The thickness of deposited films was measured by ellipsometry, and then converted to uniformity for analysis. As introduced in Chapter 4, ellipsometry offers an accurate and non-destructive way to determine the thickness and refractive index of a thin film, by means of measuring the changes in the state of polarization of collimated beams of monochromatic polarized light caused by reflection from the substrate surface. The ellipsometric measurements in this project were carried out by a Philips

PZ2000 ellipsometer. Two working modes were used in this project to examine the thickness distribution contour. One is the Raster Scan Mode. In this mode, measurements were taken at a total of 256 sites evenly distributed over a 32 × 32 mm^2 area across the 2-inch wafer with a 1.5-mm edge exclusion so as to check the overall uniformity. The other one is the Profile Scan Mode, in which the profile of the radial thickness distribution was plotted and studied. The ellipsometer measured the thickness at 30 sites with a1mm-step along the X- and Y- axes, respectively, as defined in Fig. 6.7. If not explicitly mentioned, all the expressions of "X axis, Y axis, X direction, Y direction" in this thesis are referred to the definitions illustrated in Fig. 6.7.

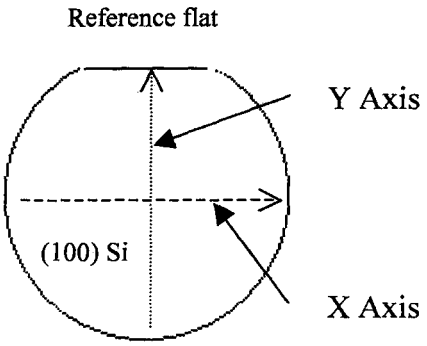

Fig. 6.7 Definition of X- and Y-axis for profile scans. X-axis is defined as a direction that passes the center and is parallel to the reference flat on a (100) Si wafer. The Y-axis passes the center and is perpendicular to X-axis.

In all the experiments we used 2-inch single side polished, (100) silicon wafers. Oxygen (10% O_2 in Ar), nitrogen (10% N_2 in Ar) and SiH_4 (30% SiH_4 in Ar) were chosen as chemical reaction precursors to produce silicon oxide (SiO_x) thin films. All the calibrations were based on the ICP deposition of SiO_x. The following measurements were taken throughout the experiments, in an attempt to minimize errors:

- Thorough sample cleaning prior to deposition as described in 5.2.1,
- Samples were sent to ellipsometric measurements immediately after the deposition,
- Every measurement was repeated a few times and an average of measured values was taken as the result.

In ICP-CVD, a lot of factors can influence the deposition. Some of these factors are constrained by the system design while others could be optimized to improve the samples characteristics, such as the uniformity of thickness. In this study the effect of a wide range of deposition parameters, such as the deposition time, distance between the sample and the plasma gun, O_2/SiH_4 gas flow ratio, oxygen gas flow rates, substrate temperature, and RF forward power, on the uniformity of thickness of deposited thin films was investigated.

6.4.1 Effect of Deposition Time

Three groups of samples were made to study the influence of deposition duration on the uniformity of thickness across the whole wafer. For group 1, two silicon oxide thin film samples were deposited under the same conditions, except deposition duration. Sample-1a deposited for 17 minutes yielded a thin film with thickness of 529Å and uniformity of 0.86%, and sample-1b for 32 minutes with thickness of 992Å and uniformity of 0.74%. Similarly, for group 2, the thin film thickness of sample 2a was 465Å, uniformity 0.63%, 2b thickness 1108Å, uniformity 0.53%; For group 3-3a, 480Å thick, uniformity 0.86%, 3b, 1082Å thick, uniformity 0.48%. These are summarized in Table 6.1.

Table 6.1 Process conditions and measured results for Groups 1,2,3

Group		Common Conditions	Deposition Time (min)	Average Thickness (Å)	Uniformity (%)
1	1a	Gas flow rate: O_2 20sccm, SiH_4 5sccm Heater Temp: 300°C RF power: 250W Sample-plasma gun distance: 140 mm	17	529±5	0.86
	1b		32	992±5	0.74
2	2a	Gas flow rate: O_2 20sccm, SiH_4 5sccm Heater Temp: 300°C RF power: 250W Sample-plasma gun distance: 160 mm	17	465±6	0.63
	2b		37	1108±6	0.53
3	3a	Gas flow rate: O_2 20sccm, SiH_4 5sccm Heater Temp: 300°C RF power: 250W Sample-plasma gun distance: 150 mm	17	480±6	0.86
	3b		35.4	1082±7	0.48

The results indicate that the deposition time has only very little influence on the uniformity of thickness over a 2-inch wafer.

6.4.2 Effect of Distance Between the Sample and the Plasma Gun

The distance between the plasma gun and the sample was found critical in affecting the uniformity of thickness across the whole wafer during the calibration. Fig. 6.8 illustrates a schematic of precursor gases injection in the ICP-CVD system.

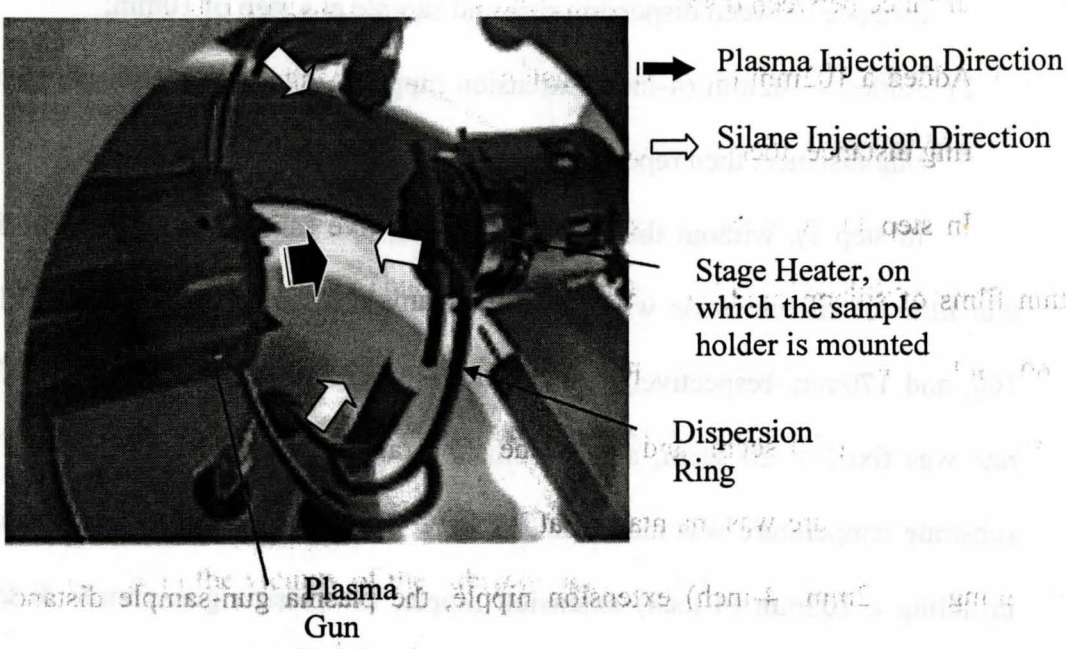

Fig. 6.8 Schematic of precursor gases injections in the ICP-CVD system

In Fig. 6.8, plasma gases O_2/Ar flow leftwards through many small holes in an aperture pattern into the main chamber, while the silane gas is injected through several tapered nozzles in a dispersion ring located in the middle of the main chamber In the ICP-CVD system, the distance from the dispersion ring to the sample is designed to be adjustable in a range of 0 ~ 37mm. Since the plasma gun is assembled on a flange with a fixed distance to the dispersion ring, an extension nipple was installed onto the flange for stepless adjustment of the distance between the plasma and the dispersion ring.

A number of experiments were carried out following the two steps as below·

1) Keeping the plasma gun-dispersion ring distance constant, adjusted the distance between dispersion ring and sample at a step of 10mm;
2) Added a 102mm (4-inch) extension nipple to change the Gun-Dispersion ring distance, then repeated step 1.

In step 1), without the extension nipple, on five samples were deposited thin films of silicon oxide with a plasma gun-sample distance of 133, 140,150, 160, and 170mm, respectively. For all of the five depositions, the oxygen flow rate was fixed at 20 sccm, and the silane flow rate was fixed at 5 sccm. The substrate temperature was maintained at 121±1°C for all the cases. In step 2), by installing a 102mm (4-inch) extension nipple, the plasma gun-sample distance was extended to 235, 242, 252, 262, and 272 mm, respectively. Other conditions were the same as in step 1). Results are shown in Fig. 6.9.

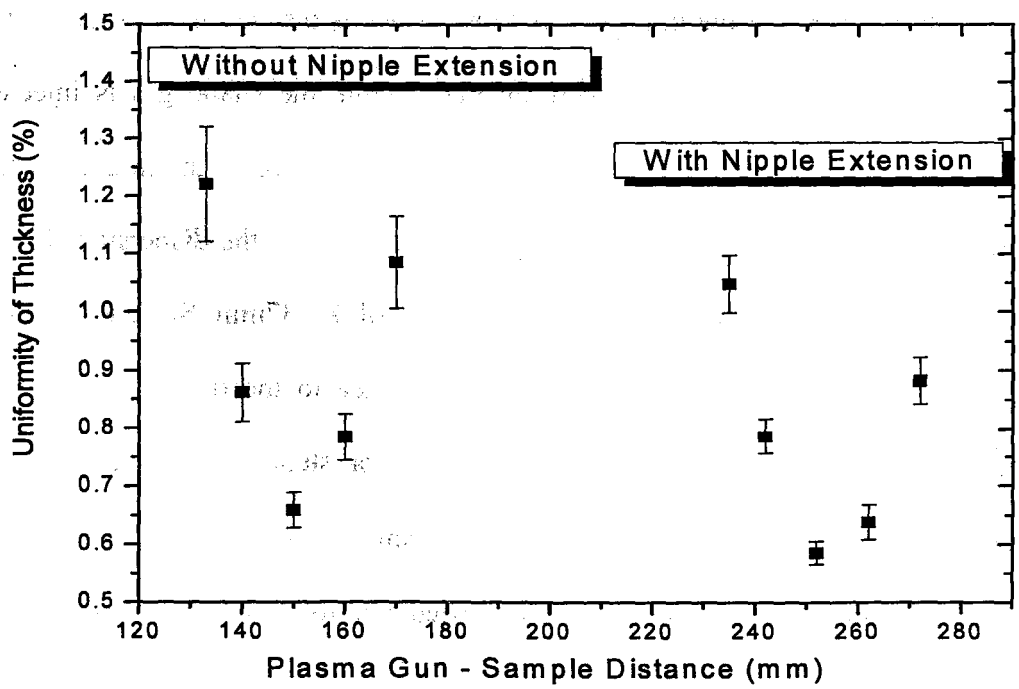

Fig. 6.9 The uniformity of thickness as a function of the distance between the sample and the dispersion ring

From Fig. 6.9 two important observations can be made. Firstly, extending the plasma gun-sample distance seems to help improve the uniformity of thickness of the deposited thin films. Secondly, in the above two cases (with and without extension), the minimum the uniformity of thickness corresponds to the same position, implying that the optimal distance between dispersion ring and sample is around 61mm. This is in accordance with the spatial distribution characteristics of a plasma flux. It is known that the plasma flux distribution is more uniform along the flowing direction and the addition of the extension nipple increases the distance from the plasma source to the substrate surface. Thus the plasma flux in the vicinity of the substrate surface is more uniform, giving rise to a more uniform thin film deposition.

Although the uniformity appears to be better when we extended the sample-gun distance by 4 inches, the shape of the deposition layer is not exactly what we expected. Let us take the point shown in Fig. 6.9 with the best uniformity as an example. The corresponding sample-plasma gun distance is 252 mm. The left graph in Fig. 6.10 shows a 3-D thickness distribution on the sample surface. A valley can be seen clearly in the middle of the deposited layer. The two curves on the right side are profiles of the layer surface along the X- and Y- axes respectively, which further show the depth of the valley is around 13 Å.

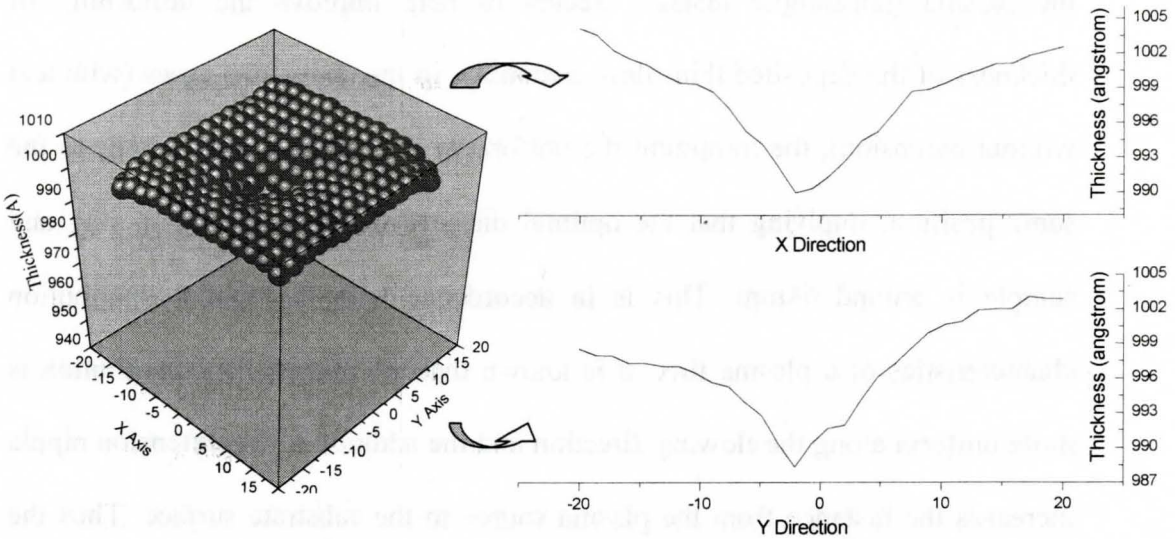

Fig. 6.10 A valley in the center of the deposited thin film

Other depositions at various plasma gun-sample distances have been tried. It seemed that although changing the plasma gun-sample distance couldn't completely eliminate the valley, there might be some improvements. Further study revealed that the valley was mainly caused by other factors, such as the oxygen flow rate, as will be discussed later For this work, only one extension nipple with a 4-inch thickness was used. Although it turned out to be useful, further study is required to find out the optimal distance between the plasma gun and the sample.

6.4.3 Effect of Aperture Patterns

We currently have three kinds of aperture patterns #1, #2 and #3, which are shown in Fig. 6.11

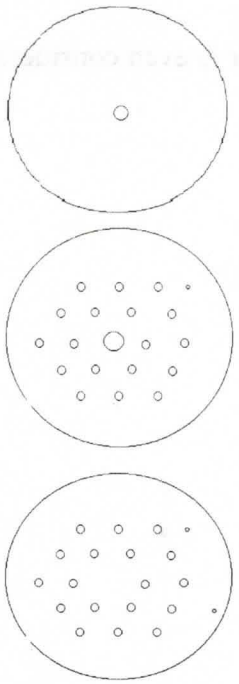

Aperture Pattern #1: one big hole with a diameter of 1mm in the center, surrounded by 30 holes×0.5mm

Aperture Pattern #2: one big hole with a diameter of 2mm in the center, surrounded by 18 holes ×1mm and 26 holes × 0.5mm.

Aperture Pattern #3: no big hole in the center, 18 holes ×1mm and 26 holes × 0.5mm.

Fig. 6.11 Three aperture patterns used in the project

Using aperture pattern #1, three depositions at three different plasma gun-sample distances were tried. Other conditions were kept constant for the three trials, which included a fixed O_2/SiH_4 flow ratio of 20/5, and a substrate temperature of 121±1°C.

Replacing aperture pattern #1 with aperture pattern #2 and #3 respectively, under the same conditions as above, two groups of six depositions were made for studying the effects of the aperture pattern on the uniformity of thickness across the whole wafer

Fig. 6.12 indicates that, while the aperture pattern #3 gives the best results, the aperture pattern doesn't have too much of an effect on the uniformity of

thickness of deposited thin films. All the uniformities obtained with the three aperture patterns are better than 1%, which is acceptable, or is even considered to be quite good.

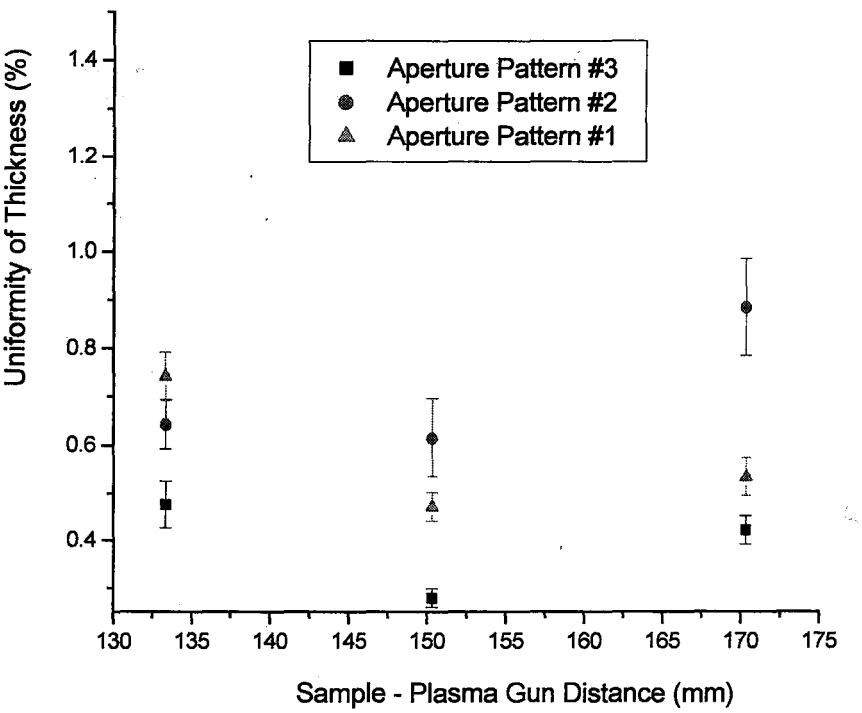

Fig. 6.12 Effect of aperture patterns on the uniformity of thickness

During the course of the experiments, aperture pattern #2 was found to be capable of producing a stable plasma even at a very low O_2/Ar flow rates, such as 5sccm. When the aperture pattern #3 was used, the plasma started to be unstable when the O_2/Ar flow rate was below 15sccm, and some intermittent sparkles were observed in the main chamber, which was considered to be caused by discharging between the plasma and the metal components (i.e. the wall and the shutter) in the chamber. When the O_2/Ar flow rate was further decreased to 8 sccm, plasma

couldn't enter into the main chamber as observed. Aperture pattern #2 behaved moderately in between. It seemed that the big hole in the center of the aperture pattern played an important role in regulating the plasma flux, especially in the case of low gas flow rates. Initially we tended to consider that the big hole might be the main reason that gave rise to the formation of a valley in the middle of deposited film, assuming that more plasma species flowing out of the big hole impinged on the sample surface, leading to a valley in the center. Experiments proved that our speculation was not correct. No matter which aperture pattern we used, all the samples had a valley in the center. Furthermore, if other experimental conditions were the same, the depths of the valleys were also very close, except that samples using the aperture pattern #3 tend to have a shallower valley compared with those using the other two aperture patterns. This result is actually coincident with the theory introduced in Chapter 2. In a plasma chamber, plasma radicals are usually confined in a circumferential ring, which is close to the wall of the chamber. In the center of the plasma chamber are just neutral gas molecules. So the species flowing out of the big hole in the aperture pattern are mainly neutral molecules with low energy, which are impossible to cause a valley in the center of the deposited film.

In conclusion, we prefer to use aperture pattern #3 for deposition because it demonstrated improved uniformity of thickness across the whole wafer and a reduction of the depth of the valley in the center of deposited films, though the improvement was not considerable.

6.4.4 Effect of Oxygen: Silane Flow Rate Ratio

In the ICP deposition of SiO_2, as reported for other PECVD deposited SiO_2, the most significant factor determining the quality of the material is still the oxygen to silane gas flow ratio [1]. To study the influence of oxygen to silane gas flow ratio on the uniformity of thickness, two groups of comparative experiments were carried out in the ICP-CVD system. Shown in Fig. 6.13 are the experimental results.

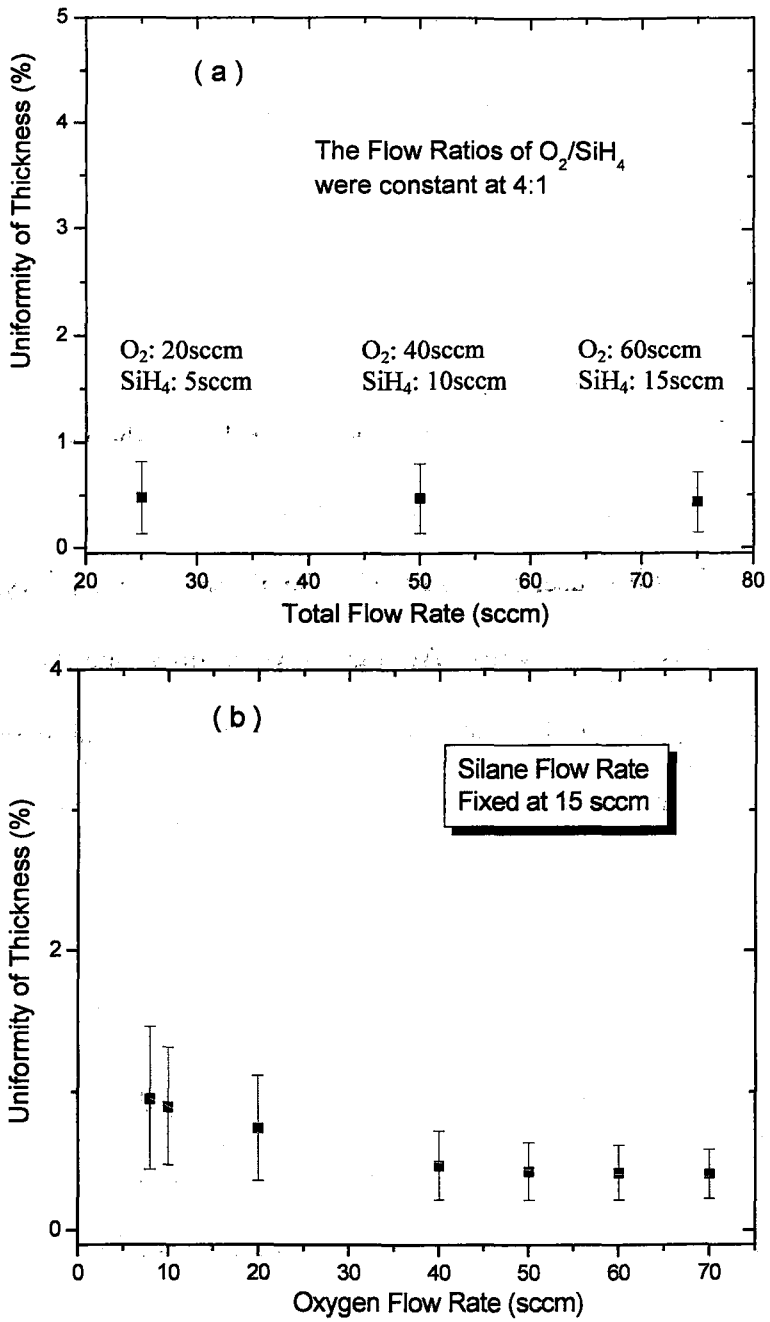

Fig.6.13 Effect of flow ratio of oxygen to silane on the uniformity of thickness. In (a) the flow ratios of oxygen/silane were constant at 4:1. In (b), the oxygen flow rate changed from 8 to 70 sccm with a constant silane flow rate of 15 sccm.

For the first group, I used three pairs of O_2 and SiH_4 flow rates, 60/15, 40/10, and 20/5 with the same ratios of O_2 to SiH_4 flow rates. Although the total oxygen and silane flow rates were different in these three depositions, the plot of the uniformity of thickness vs. flow ratio of O_2 /SiH_4 in Fig. 6.13 (a) clearly indicates that they contribute the same to the uniformity of thickness.

In the second group, seven O_2 /SiH_4 flow ratios of 8/15, 10/15, 20/15, 40/15, 50/15, 60/15 and 70/15 were used. Fig. 6.13 (b) shows that the uniformity of thickness across the deposited film is getting better as the flow ratio of O_2 /SiH_4 increases. This is because, compared with the silane precursor, oxygen radicals in the plasma have more energy. At high oxygen flow rates, excessive oxygen radicals impinging on the substrate surface have a probabilistic tendency to smoothen the surface. While at low oxygen flow rates, SiH_n particles dominate in the environment above the substrate surface. The smoothening ability of SiH_n particles is not as strong as oxygen particles in the plasma due to a lower energy, causing a worse uniformity of thickness than at high oxygen flow rate.

At the O_2 /SiH_4 flow ratio of 70/15, the deposited SiO_2 thin films turn out to have a better uniformity of thickness than at the O_2 /SiH_4 flow ratio of 10/15, however the contour of the thickness distribution of the both cases is different. Fig. 6.14 illustrates the influence of the flow rate ratio of O_2/SiH_4 on the thickness profile along X- and Y- axes.

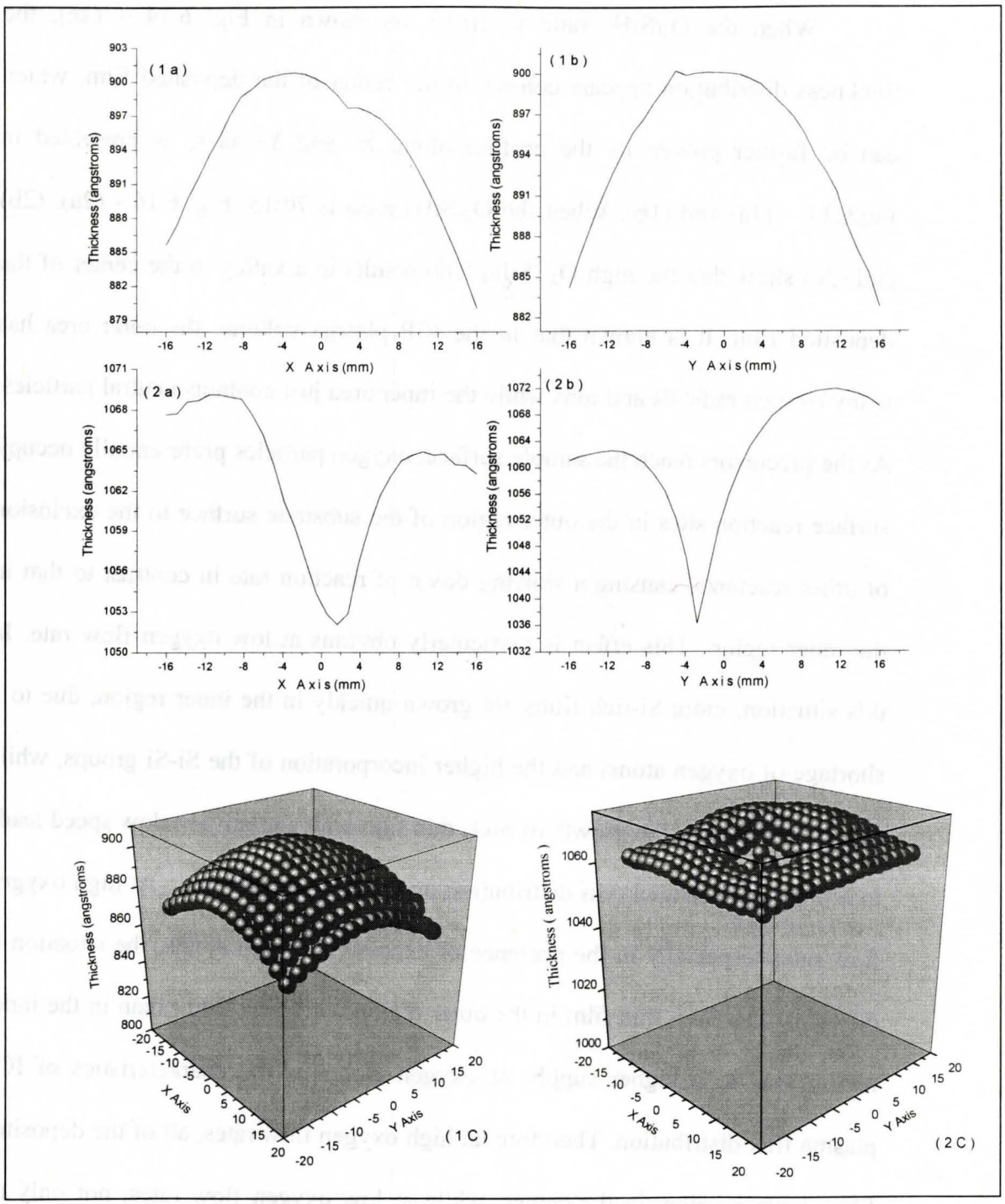

Fig. 6.14 The influence of the flow rate ratio of oxygen to silane on the thickness profile. In group (1), O_2:SiH_4 = 10:15, in group (2), O_2:SiH_4 = 70 15

When the O_2/SiH_4 ratio is 10/15, as shown in Fig. 6.14 – (1c), the thickness distribution appears convex in the center of the deposited film, which can be further proven by the profiles along X- and Y- axes, as presented in Fig.6.14 – (1a) and (1b). When the O_2/SiH_4 ratio is 70:15, Fig. 6.14 - (2a), (2b) and (2c) show that the high O_2 /SiH_4 ratio results in a valley in the center of the deposited film. It is known that in the ICP plasma volume, the outer area has many oxygen radicals and ions while the inner area just contains neutral particles. As the precursors reach the sample surface, oxygen particles preferentially occupy surface reaction sites in the outer region of the substrate surface to the exclusion of other reactants, causing a slowing down of reaction rate in contrast to that in the inner region. This effect is particularly obvious at low oxygen flow rate. In this situation, more Si-rich films are grown quickly in the inner region, due to a shortage of oxygen atoms and the higher incorporation of the Si-Si groups, while in the outer region, the growth of SiO_x thin film with a relatively slow speed leads to a final hill-like thickness distribution on the substrate surface. At high oxygen flow rates, especially in the presence of excessive oxygen atoms, the situation is different. The SiO_2 thin film in the outer region will grow faster than in the inner region, due to a higher supply of oxygen atoms as the characteristics of ICP plasma flux distribution. Therefore, at high oxygen flow rates, all of the deposited films have a valley in the center, while at low oxygen flow rates, not only no valley is observed, but also a convex stage appears in the center of the deposited film.

6.4.5 Effect of the Substrate Temperature

Temperature is one of the most important factors that influence the growth and quality of thin films produced by CVD methods. ICP-CVD uses an ICP source to produce high-density plasma for enhancement and reduce the deposition temperature to nearly room temperature, however the temperature factor was still found in our experiments to somewhat affect the thickness distribution on the deposited thin film.

How the deposition temperature influences the uniformity of thickness is shown in Fig. 6.15.

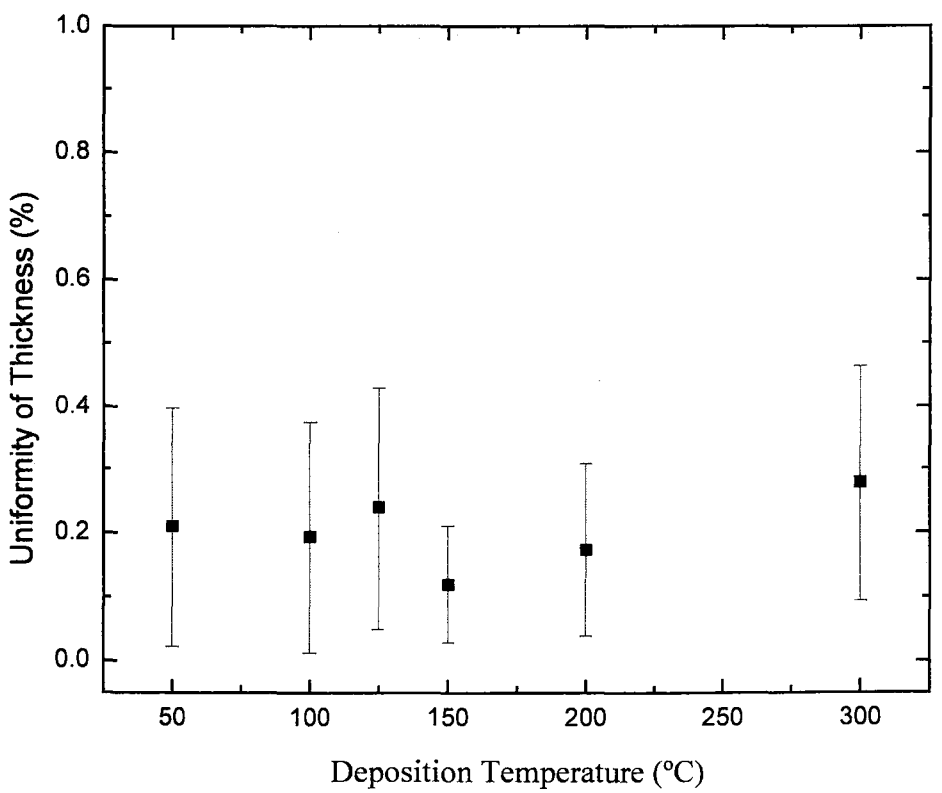

Fig. 6.15 Effect of deposition temperature on the uniformity of thickness

The O_2/SiH_4 flow ratio was fixed at 60:15. The plasma gun-sample distance was set at 150 mm. Six comparative depositions were done at the temperatures of 50, 100, 125, 150, 200, and 300°C respectively (The corresponding substrate temperatures are 38, 55, 63, 71, 88, and 121°C, respectively, based on the temperature calibration described in section 6.2. The uncertainty in these values is ±1°C.). It appears that the deposition temperature has a weak influence on the uniformity of thickness as shown in Fig. 6.15. But Fig. 6.16 indicates that the temperature apparently affects the shape of thickness distribution. When the temperature is below 150°C, the sample surface demonstrates a convex profile. Above that point, a valley appears in the center of the deposited film, and the valley becomes deeper as the temperature increases from 150 to 300°C. The phenomenon is believed to relate to the temperature distribution characteristics of the heater based on that fact that particles are more active at higher temperatures. Chemical reactions at the sites where the temperature is high occur more intensively, leading to a faster growth of SiO_2 films there. As introduced in Chapter 3, the stage heater in the ICP-CVD system consists of a planar, multi-turn spiral coil resistive heating element, which is designed to offer an evenly distributed heating to the substrate. It appears that a perfect even-temperature distribution across the whole wafer is not available in our system. There seems to be a threshold near 150°C: above that point, the heater creates a temperature distribution, high on the outside and low on the inside and vice versa below that point. This temperature distribution feature explains the

experimental results shown in Fig. 6.16. Bt the effect caused by this fluctuation is restricted to somewhat influence the shape of the thickness distribution, while the influence on the uniformity ıs negligible.

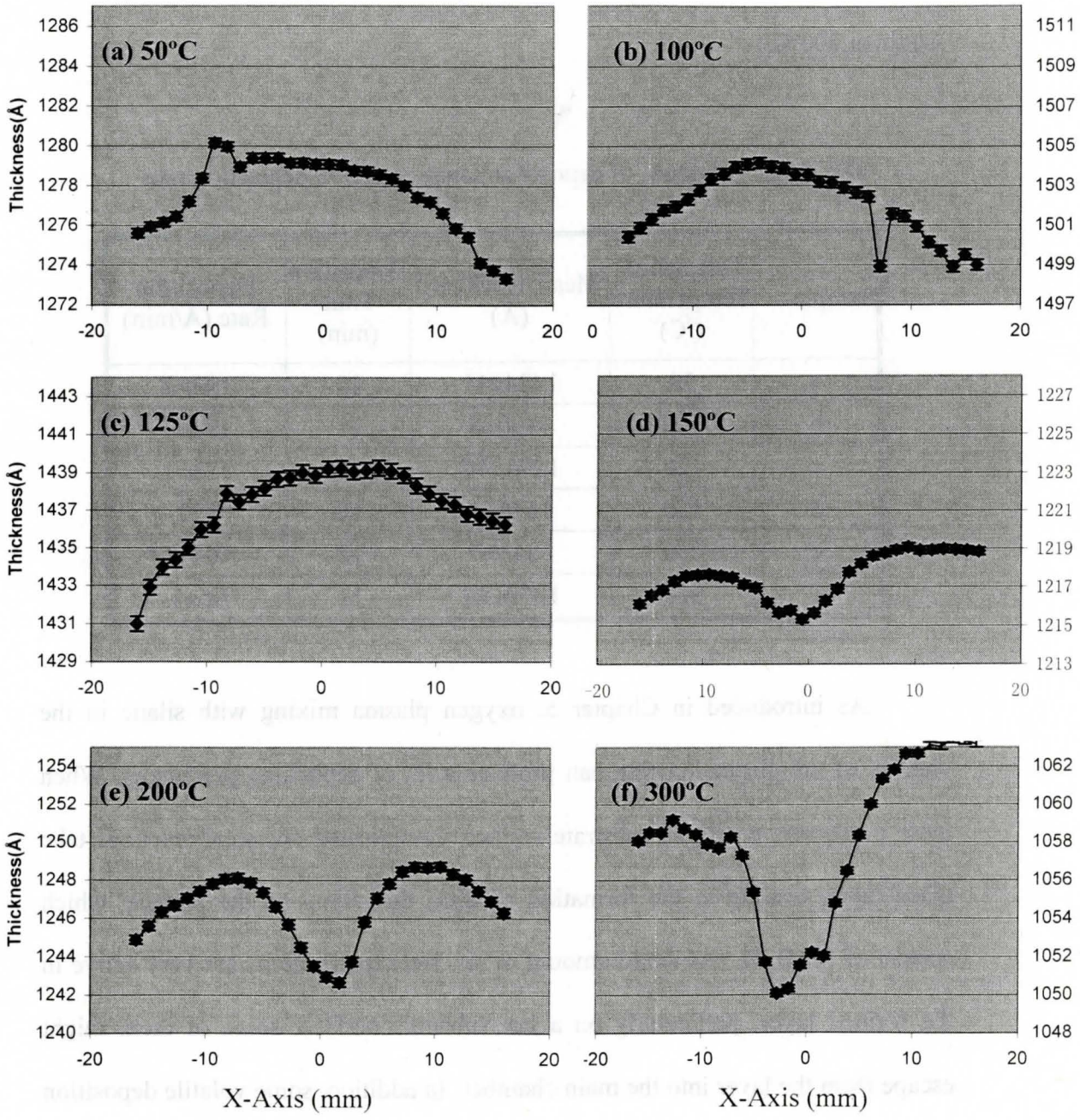

Fig. 6.16 Effect of deposition temperature on the thickness profile along a direction cross the center of the wafer

Table 6.2 summarizes the temperature influence on the deposition rate. The deposition rate appears to be inversely proportional to the deposition temperature, i.e. the deposition rate decreases with the increasing temperature. The change in range is as high as 49%, from 143 Å/min at room temperature to 96 Å/min at 300°C.

Table 6.2 Influence of deposition temperature on deposition rate

Sample	Deposition Temperature (°C)	Mean Thickness (Å)	Deposition Time (min)	Deposition Rate (Å/min)
a	50	1434±11	10	143±1
b	100	1499±8	11	136±1
c	125	1275±10	10	128±1
d	150	1216±4	10	122
e	200	1245±7	12	104±1
f	300	1059±10	11	96±1

As introduced in Chapter 5, oxygen plasma mixing with silane in the vicinity of the dispersion ring can produce a lot of deposition precursors. When these precursors reach the substrate surface, complicated chemical reactions take place there, leading to the formation of SiO_2 thin films on the surface, which consist of Si, O, H, and small amount of Ar. Because H atoms are very active in the formed layer, particularly on a hot substrate surface, some of them might escape from the layer into the main chamber. In addition, some volatile deposition precursors are likely to be evaporated from a hot surface and removed by vacuum

pumping. These effects will cause a slowdown of the deposition rate. The higher the temperature is, the more significant this effect will be. So, at low deposition temperature, the deposition rate is high, but the content of hydrogen in the deposited film is also high. Similarly higher deposition temperatures lead to a lower deposition rate but also a lower density of hydrogen concentration in the film.

In general, based on above analysis, we found that although the shape of thickness distribution is not the best, the thin films deposited at 300°C turn out to have a good uniformity at an acceptable deposition rate (96 Å/min) with lower hydrogen concentration (which have not yet been verified by ERD measurement). So, from the perspective of the uniformity of thickness and the deposition rate, a deposition temperature around 300°C (resulting in a sample temperature of 121±1°C) is recommended in the ICP-CVD deposition.

6.4.6 Effect of RF Power

The RF power influences the film properties by activating and dissociating precursors and providing ions that bombard the deposited thin film. How the RF power affects the thin film uniformity is shown in Fig. 6.17, with the O_2/SiH_4 flow ratio fixed at 20:5, the sample-plasma gun distance set at 150 mm, and the deposition temperature maintained at 300°C. The thin film deposited at 500W shows a rougher surface and a worse uniformity compared with that deposited at 250W. This result is consistent with our expectation. Since high RF power is likely to increase the energy of radicals in the plasma, so the uniformity of

thickness across the whole wafer will get worse as a result of strong radical bombardments to the film surface at fairly high RF power. Further calibrations regarding this issue revealed that a RF power in the range of 250 ~350W is suitable for depositing thin films in this ICP-CVD system, with good the uniformity of thickness and an acceptable growth rate.

Experimental Conditions:

Flow rate: SiH_4 5sccm

O_2/Ar 20sccm

Deposition Temp: 300 °C

Sample-Plasma Gun

Distance: 150mm

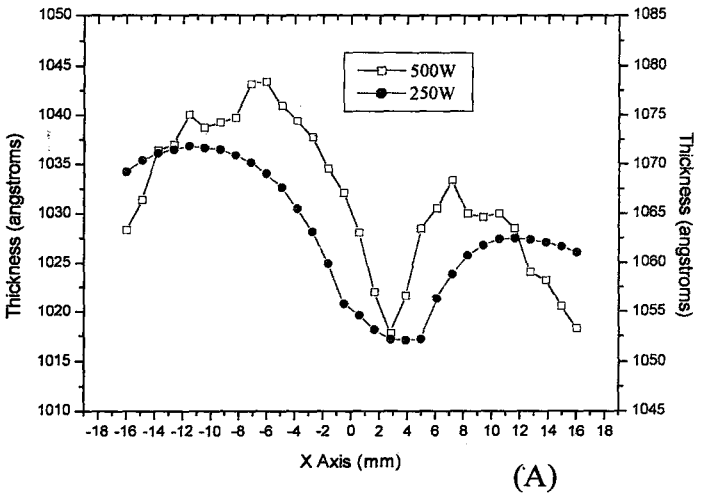

(A)

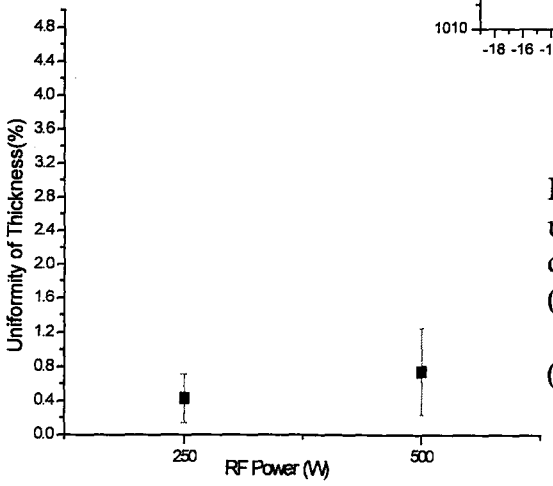

(B)

Fig. 6.17 Effect of RF power on the uniformity of thickness and the distribution contour.
(A) Along-X-axis profiles of thin films deposited at 250W and 500W.
(B) Plot of the uniformity of thickness vs. RF power

6.5 Refractive Index

The most significant factor determining the optical characteristics (e.g. refractive index) of ICP-CVD-fabricated thin films was found to be the oxygen to

silane gas flow ratio. In order to investigate the dependence of refractive index on the oxygen-to-silane flow ratio, a series of 22 experiments were carried out under the following conditions:

For all of the experiments, the silicon precursor, which is a mixture of 30% SiH_4 in Ar, was kept at a constant flow rate, 15 sccm. A mixture of 10% O_2 in Ar was used as the plasma gas precursor. By using the mixture of 10% oxygen in argon, a fine control of the oxygen flow rate of 0.1sccm was possible. The flow rate of Ar-diluted oxygen varied in a range from 1 to 80 sccm. So the total gas flow rate during deposition was between 16 and 95sccm. The RF forward power was tuned together with the reflected power until a net power of 300W was coupled into the plasma. The heater's temperature was set at 350°C, thus obtaining a substrate temperature of 137°C.

Fig. 6.18 shows the dependence of the film refractive index on the oxygen/silane flow ratio.

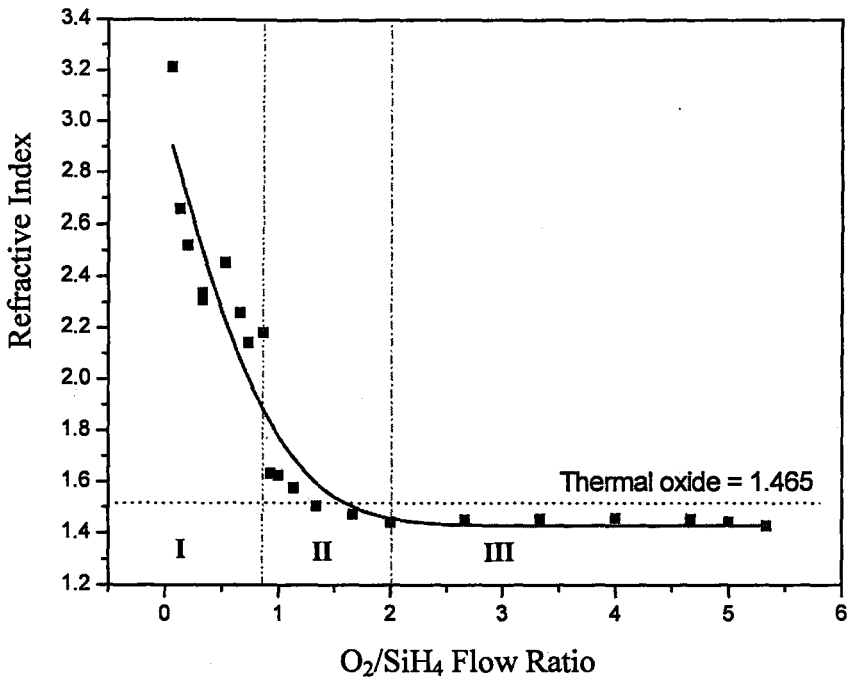

Fig. 6.18 Refractive index as a function of the oxygen to silane flow ratio

Just as expected, the refractive index, n decreases with increasing flow ratio, indicating that the films change from Si-rich to O-rich. We know that stoichiometric thermal oxides have n ~ 1.46, whereas Si-rich films have n > 1.46 and O-rich films have n < 1.46. As shown in Fig. 6.18, the red curve is a Gaussian-fit trend. The overall curve can be divided into three sections.

In section III, namely for oxygen/SiH_4 ratios above 2, the refractive index n remains nearly constant, $n = 1.453 \pm 0.002$, indicating that the Si:O composition is locking onto SiO_2. The reason why the refractive index (n~1.453) is a little bit less than thermal one (1.465) is probably due to some hydrogen bonded into the

deposited film. This phenomenon is very common in thin films produced by CVD, especially at low temperature. Because of the use of silane as the precursor, it is inevitable that hydrogen cannot be eliminated completely from deposited thin films. But our data is very close to that under thermal conditions, with a difference as small as 0.8%, which means that ICP-CVD is capable of growing silicon oxide thin films with very good quality at very low deposition temperatures. The small difference could be reduced to a negligible level by either increasing the deposition temperature or post-annealing.

In section II, the O_2/SiH_4 flow ratio increases from 0.9 to 2, while the refractive index decreases from 1.63 to 1.45. This is a transition region indicating that the deposited silicon oxide thin film begins to change from the silicon-rich silicon oxide (SRSO) to the pure silicon dioxide.

The O_2/SiH_4 flow ratio of 0.9 seems to be a threshold of the change of the refractive index. As can be seen from section I, even if the ratio drops by only a very small amount, e.g. 0.06 in my experiments, the refractive index will jump sharply from 1.63 to 2.17, increasing as high as 33%. From this point on, as the O_2/SiH_4 ratio decreases from 0.93 (14:15) to 0.07 (1:15), the index increases from 2.17 to 3.21, which shows a steep change of refractive index. When the oxygen/SiH_4 ratio is about 0.07 (1:15), the real ratio of pure oxygen to silane is actually 0.007. In this case, there is very little oxygen incorporation in the surface deposition process, and therefore nearly pure silicon is deposited.

Other effects, such as plasma instabilities, the substrate temperature, and the total chamber pressure, can also have some influence on the refractive index. These factors need to be considered for further exploration.

Chapter 7

Conclusions and Future Work

7.1 Conclusions

With the help of Johnsen Ultravac Inc. and SVT Associates, Inc., a new custom-designed Inductively Coupled Plasma Chemical Vapor Deposition(ICP–CVD) system has successfully been set up at McMaster University. My work focused on the system installation, maintenance and calibrations. Using 2-inch single side-polished (100) silicon wafers as the substrates, and O_2/Ar/SiH_4 as precursors, a large number of silicon oxide thin films have been deposited by ICP-CVD, in an attempt to explore the optimal deposition conditions for this system. I have successfully finished the calibrations or optimization on the temperature, minimum reflected power, thickness uniformity and the refractive index.

It was found that the substrate temperature is linearly related to the temperature of the stage heater by an empirical equation:

$$T_{substrate} = 0.3303 \times T_{stage\ heater} + 21.58\ (^{\circ}C)$$

Five gases of O_2 (99.99%), N_2 (99.999%), a nitrogen mixture (10% N_2, 90% Ar), an oxygen mixture (10% O_2, 90% Ar) and Ar (99.9%) were ignited to form plasmas at different flow rates under various RF forward powers ranging from 200 to 400W. The ICP source was found to be capable of efficiently generating a stable plasma for all the gases with a very low reflected power.

Thickness uniformity is an important factor to estimate the quality of the deposited thin film, which is subject to many factors, such as the substrate temperature, gas flow rates and ratios of O_2/SiH_4, RF power, the deposition time, the distance between the plasma gun and the sample, and the aperture pattern. In the experiments, the following conditions were found to be of great merit if a good surface uniformity of better than 1% is desired:

- The deposition temperature around 300 °C (corresponding to a sample temperature of 121±1°C);
- RF power ranging from 250W to 350W;
- The dispersion ring-sample distance kept in the vicinity of 61mm;
- Moderate flow ratio of O_2/SiH_4, such as 40/15. Higher ratio results in a valley in the center, lower ratio leads to worse uniformity.

Other factors, such as the total chamber pressure, the offset between the ICP source axis and the wafer, the rotation speed of the stage, and the offset of tilting the stage can also influence the surface uniformity of deposited thin films. Some of these are fixed by design, thus not adjustable; some have not been studied due to the time limitation, and remain to be done for future work.

The refractive index n was found to vary in a range of 1.42 ~ 3.21 as the flow ratio of oxygen to silane changed from 80:15 to 1:15. The trend that n falls with increasing flow ratio is consistent with that reported using other PECVD methods to produce SiO_x thin films. Furthermore, the refractive index of the silicon dioxide thin film as-deposited in our system is very close to that under

thermal conditions, with a difference of as small as 0.8%. This means that our ICP-CVD system is capable of growing good quality silicon dioxide thin films with at low deposition temperatures.

7.2 Future Work

In order to use this new ICP-CVD system to produce different kinds of thin films with better quality, not only further work are required to optimize the deposition conditions, a full study of the optical and electrical characteristics of deposited films is also necessary in the future. To achieve this goal, efforts are underway to address the following three aspects:

7.2.1 Continuing Calibrations

On the one hand, during the course of calibrations, I skipped some work for some reasons, which should be made up if possible. For example, the distance between the dispersion ring and the sample was steplessly changed during investigating the distance effect on surface uniformity. But the dispersion ring - plasma gun distance was just changed once using a 4-inch extension nipple. This is obviously insufficient to find out the best plasma gun-sample distance. Furthermore, the uniformity calibration is far from perfection. I ignored some factors that might influence the uniformity, e.g. the total chamber pressure.

On the other hand, the work in this thesis focused on calibrating the system for the deposition of SiO_x thin films. The existing gas system enables producing silicon nitride and silicon oxynitride thin films, which also needs to be calibrated.

7.2.2 System Improvement

A number of modifications to the system are presently underway or required in order to further improve the deposition quality and efficiency. All of the depositions in this thesis were carried out in manual mode, due to an unsuccessful communication between the RF power source and RF plasma controlling system. The system is designed to work primarily in automatic mode, aiming at reducing the human operational errors and response time. In principle, multi-layer thin films can be grown continuously in this ICP-CVD system with a desired thickness and refractive index for every layer, which are precisely controlled by an in-situ ellipsometer. To achieve this goal, a task of top priority is to fix the communication problem, followed by a careful calibration.

After many depositions, the inner wall of the main chamber is now covered by a thick layer of deposited materials. These residues attached on the chamber wall might cause unexpected negative influence on the quality of deposited thin films. Completely cleaning the main chamber, including the chamber wall, view windows, the sample holder, the manipulator, the shutter, the bulb, and all the other exposed-to-plasma components in the main chamber, is a big issue in the near future. The conventional CF_4 -based chamber cleaning is known to have some shortcomings like low gas utilization, insufficient cleaning effect and big environmental concerns. A C_2F_6-based cleaning method has recently been reported to be a good alternate candidate to effectively clear the entire residue from the main chamber. In general, a cleaning method is to be

carefully chosen from the perspective of efficiency, cost, and environment, and carried out periodically.

Ion bombardment energy at the film surface was found during the experiments to influence the uniformity as well as other film properties to some extent. It was reported [1] that negatively biasing the substrate could be used to tune the energy of ion bombardments. It provides us a possible approach to improve the thin film uniformity. Though currently not used in the ICP-CVD system, substrate biasing is not difficult to realize. This modification deserves further consideration and study.

7.2.3 Study of Optical and Electrical Properties of Deposited Films

Though some characteristics of thin films were measured during calibrations, e.g. the thickness uniformity and the refractive index, more other optical and electrical properties haven't been investigated.

First of all, the compositional and structural analysis of deposited films will be done as soon as possible. It is planned to use Nuclear Reaction Analysis (NRA) and Elastic Recoil Detection (ERD) to determine the oxygen, nitrogen and hydrogen area densities of the films. A Fourier Transform Infrared (FTIR) Spectrometer will be used to investigate the film composition and chemical bonds. The thermal stability of thin films deposited by ICP-CVD will be investigated by using rapid thermal annealing for various durations at different temperatures, then followed by NRA, ERD and FTIR measurements. Secondly, to investigate the physical properties of the films, a buffer oxide etchant (BOE)

solution which contains an mixture of HF:NH_4 (1:20) will be used to determine the wet etch rate. In addition, a polarization-resolved photoluminescence technique will be used to measure the mechanical stress of deposited films. Last but not least, the electrical properties of the films are also very important for their applications in devices, as will be studied by making a MOS capacitor based on the deposited thin film. Therefore the current-voltage (I-V) and capacitance-voltage (C-V) characteristics could be measured and plotted.

References

[1] Krishna Seshan, *Handbook of Thin Film Deposition Processes and Techniques: Principles, Methods, Equipment and Applications, Second Edition*, Published by Noyes Publications/Willan Andrew Publishing (2002).

[2] J.W. Lee, K.D.Mackenzie, D.Johnson, J.N.Sasserath, S.J. Pearton, and F.Ren, *Journal of The Electrochemical Society*, **147** (4) 1481 (2000).

[3] Cheng-Hsien Chou, Jin-Hua Huang, Yung-Chen Lin, Nyan Hwa Tai, *Integrated Ferroelectrics*, **68**: 95–103 (2004).

[4] D.R.Cote, S.V.Nguyen, A.K.Stamper, D.S.Armbrust, D.Tobben, R.A.Couti, and G.Y.Lee, *IBM J. Res. Develop.*, **43**, 1/2 (1999).

[5] J.C.Damasceno, S.S.Camargo Jr., M.Cremona, *Materials Research*, Vol. 6, No.1, 19-23 (2002).

[6] J Hopwood, *Plasma Sources Sci. Technol.* **1** 109-116 (1992).

[7] K.F.Chiu, Z.H. Barber, *J. App. Phys.* **91** (4) 1797 (2002).

[8] S.J. Yu, Z.F. Ding, J. Xu, J.L. Zhang, T.C. Ma, *Thin Solid Films* **390** 98-103 (2001).

[9] S. Ashida, M.R. Shim, M.A. Lieberman, *J. Vac. Sci. Technol.* A **14** (2) 391 (1996).

[10] Keller J H, Bull. *Am. Phys. Soc. Series II* **34** (1989).

[11] Ventzek P L G, Hoekstra R J, Sommers T J and Kushner M J, *Appl. Phys. Lett.* **63** 605 (1993).

[12] Treichel H, Braun R, Gabric Z, Spindler O, Gschwandtner A., *J. Phys. IV,* **1,** 839-46 (1991).

[13] Bartle DC, Andrews DC, Grange JD, Harris PG, Trigg AD, Wicknden DK. *Vacuum*, **34** : 315 - 20 (1984).

[14] Sze SM. *VLSI Technology,* Auckland: McGraw-Hill International, p.119-21 (1986).

[15] Kruger M, Arens-Fisher R, Thonissen M, Munder H, Berger M, Luth H. *Thin Solid Films* **276**, 257-260 (1996).

[16] Barbour JC, Stein HJ, Popov OA, Yonder M, Outten CA. *J. Vac. Sci. Technol.* A **4** 480-489 (1991).

[17] Kobayashi I, Ogawa T, Hotta S., *J. Appl. Phys.,* **42**,331-336 (1992).

[18] M.B. Yu, Rusli, S.F. Yoon, S.J. Xu, K. Chew, J. Cui, J. Ahn, Q. Zhang, *Thin Solid Films* **177-181**, 377-378 (2000).

[19] J.H. Shim, Seongil Im, N.H. Cho, *Applied Surface Science* **234** 268–273 (2004).

[20] Winge R.K., *ICP–Atomic Emission Spectroscopy*, Elsevier Science Pub. Co. (1985).

[21] Hill, Sleve J., *Inductively Coupled Plasma Spectroscopy and Its Applications*, Sheffield Academic Press (1999).

[22] John H Keller, *Plasma Sources Sci. Technol.* **5**, 166-172 (1996).

[23] R.J. Goldston, and P.H. Rutherford, *Introduction to Plasma Physics*: Institute of Physics Publishing, Bristol, England (1995).

[24] Chapman, Brian N, *Glow Discharge Processes: Sputtering and Plasma Etching*, New York: Wiley (1980).

[25] Michael A. Lieberman and Allan J. Lichtenberg, *Principles of Plasma Discharges and Materials Processing*, Second edition, John Wiley and Sons, Inc. (2005).

[26] Anatoly P Nefedov, *Plasma Sources Sci. Technol.* **11** A38–A41 (2002).

[27] M J Goeckner ,J. Goree, and T. E. Sheridan, *Phys. Fluids*, B **4** (6), June (1992).

[28] Kazimierz Albinskiy, Karol Musio, Adam Miernikiewiczy, Stefan Labuzz and Marek Malota *Plasma Sources Sci. Technol.* **5** 736–742 (1996).

[29] G.S.Anderson,W.N.Mayer, and G.K.Wehner, *J. App. Phys.* **33**, No.10, 2991-2992 (1962).

[30] Annemie Bogaerts, Erik Neyts, Renaat Gijbels and Joost van der Mullen, *Spectrochimica Acta Part B: Atmic Spectroscopy*, Vol. 57 (4), 609-804, 5 Apr. (2002).

[31] Popov, O.A., *High Density Plasma Sources - Design,Physics and Performance*, William Andrew Publishing/Noyes (1995).

[32] W. Hittorf, *Wiedemanns. Ann. Phys.* **21**, 90 (1884).

[33] Townsend J.S., and Donaldson R.H., *Phil. Mag.* **5**, 178 (1928).

[34] Gabat, G.I., *J. Inst. Elect. Eng.*, Part III, **94** (27), 27-37 (1947).

[35] J.W.Denneman, *J.Phys. D:* Appl. Phys. **23** 293-298 (1990).

[36] T Intrator and J Menard, *Plasma Sources Sci. Technol.* **5** 371-382 (1996).

[37] R A Stewart, P Vitello, D b Graves, E F Jaeger, and L A Berry, *Plasma Sources Sci. Technol.* **4** 36-46 (1995).

[38] J T Gudmundsson, and M A Lieberman, *Plasma Sources Sci. Technol.* **6** 540-550 (1997).

[39] Godyak V A, Piejak R B and Alexandrovich B M, *Plasma Sources Sci. Technol.* **3** 169-176 (1994).

[40] Pascal Colpo, Roland Ernst, F.Rossi, *J. App. Phys.* **85** (3) 1366-1371 (1999).

[41] Badri Ramamurchi, Demetre J E Economou and Igor D Kaganovich, *Plasma Sources Sci. Technol.*, **12**, 302-312 (2003).

[42] Gilles Cunge, Brendan Crowley, David Vender and Miles M Turner, *Plasma Sources Sci. Technol.*, **8**, 576-586 (1999).

[43] Kortshagen U, Gibson N D and Lawler J E, *J. Phys. D :* Appl. Phys. **29** 1224-36 (1996).

[44] J. Amorim, H.S. Maciel, and J.P. Sudano, *J.Vac. Sci. Technol.* B **9** (2), Mar/Apr (1991).

[45] Granville-Phillips, Model 360 and 316 *vacuum gauge controller system.*

[46] SVT Associates, Inc., Robo-RF 3.0 *Plasma Control system and Model RF 6.02 Plasma Source User Manual.*

[47] A. Montaser, *Inductively Coupled Plasma Mass Spectrometry*, Wiley, New York (1998).

[48] Ronald R. Willey, *Practical Design and Production of Optical Thin Films*, Marcel Dekker, Inc., New York (1996).

[49] Edwards, *Model EO9K.*

[50] Leybold, *RUVAC WA251.*

[51] M.G.Boudreau, Master's thesis, McMaster University (1993).

[52] Balzers, *ModelTMH261.*

[53] M. Hablanian and K. Caldwell, *The Overload Conditions in High-Vacuum Pumps*, Proceedings of the 34th Annual Technical Conference of the Society of Vacuum Coaters, SVC Publications, pp.253 (1991).

[54] Marsbed Hablanian, *High-Vacuum Technology—A Practical Guide*, Chapter 6, Marcel Dekker, Inc., New York (1990).

[55] P. Drude, *Annalen der Physik,* **1**, 566 (1900).

[56] P. Drude, *Annalen der Physik*, **3**, 369 (1900).

[57] K. Vedam, *Spectroscopic Ellipsometry: A Historical Overview*, Thin Solid Films, 313-314 (1998).

[58] J.A.Woollam Co. Inc., *Guide to using WVASE32®: a short course in ellipsometry.*

[59] David S. Kliger, James W.Lewis and Cora Einterz Randall, *Polarized Light inOptics and Spectroscopy*, Academic Press Inc., New York (1990).

[60] John A. Woollam, Blaine Johs, etc., *Overview of variable angle spectroscopic ellipsometry, Part I: Basic Theory and Typical Applications*, Critical Review of Optical Science and Technology, CR72:3 (1999).

[61] Edward D.Palik, ed. *Handbook of Optical Constants of Solids*, Academic Press, Inc., New York (1985).

[62] H. Arwin, *Spectroscopic Ellipsometry and Biology: Recent Development and Challenges*, Thin Solid Films, 313-314: 764 (1998).

[63] F.Ferrieu and J.H.Lecat, *Journal of the Electrochemical Society*, **137**: 2203 (1990).

[64] Philips, *SD 400x/200x/230x/210x (LA) – Thin Film Measurement System (System Manual)*, Chapter 4.

[65] M.G. Boudreau, S.G.Wallace, G.Balcaitis, S.G.Murugkar, H.K. Haugen, and P. Mascher, *App. Opt.* **39**, 1053 (2000).

[66] P. Mascher, J. Wojcik, *Electrochem. Soc. Proc.* **2002-4**, 3-22 (2002)

[67] A Dollet, J P Couderc and B Despax, *Plasma Sources Sci. Technol.* **4** 94-106 (1995).

[68] G. lucovsky, P.D. Richard, D.V. Tsu, S.Y. Lin, and R.J. Markunas, *J.Vac.Sci. Technol.* A **4** (3), May/Jun (1986).

[69] G. Turban, *Pure & Appl. Chem.* **56**, No. 2, 215-230 (1984)

[70] P. A. Longeway, R. D. Estes, and H. A. Weakliem *J. Phys. Chem.*, **88**, 73-77 (1984).

[71] Mark J. Kushner, *J. Appl. Phys.* **74** (11), 1 December, 6538-6553 (1993).

[72] D.V.Tsu, G. N. Parsons, G. Lucovsky, and M. W. Watkins, *J. Vac. Sci. Technol.* A **7**, 1115 (1989).

[73] J. A. Thiel, D. V. Tsu, M. W. Watkins, S. S. Kim, and G. Lucovsky, *J. Vac. Sci. Technol.* A **8**, 1374 (1990).

[74] Sergei E. Alexandrov, Alexei Yu Kovalgin, *Adv. Mater. Opt. Electron.*, **8**, issue 1,13-22 (1998).

346026